University of Groningen

Future evolution of bound superclusters in an accelerating Universe

Araya-Melo, Pablo A.; Reisenegger, Andreas; Meza, Andres; van de Weygaert, Rien; Duenner, Rolando; Quintana, Hernan

IMPORTANT NOTE: You are advised to consult the publisher's version (publisher's PDF) if you wish to cite from it. Please check the document version below.

Document Version
Publisher's PDF, also known as Version of record

Publication date:
2009

[Link to publication in University of Groningen/UMCG research database](#)

Future evolution of bound superclusters in an accelerating Universe

Pablo A. Araya-Melo,[1,2,3]★ Andreas Reisenegger,[4] Andrés Meza,[5]
Rien van de Weygaert,[1] Rolando Dünner[4] and Hernán Quintana[4]

[1]*Kapteyn Astronomical Institute, University of Groningen, PO Box 800, 9700 AV Groningen, the Netherlands*
[2]*Korea Institute for Advanced Study, Dongdaemon-gu, Seoul 130-722, Korea*
[3]*Jacobs University Bremen, Campus Ring 1, 28759 Bremen, Germany*
[4]*Departamento de Astronomía y Astrofísica, Facultad de Física, P. Universidad Católica de Chile, Casilla 306, Santiago 22, Chile*
[5]*Departamento de Ciencias Fisicas, Facultad de Ingenieria, Universidad Andres Bello, Santiago, Chile*

ABSTRACT

The evolution of marginally bound supercluster-like objects in an accelerating Λ cold dark matter (ΛCDM) Universe is followed, by means of cosmological simulations, from the present time to an expansion factor $a = 100$. The objects are identified on the basis of the binding density criterion introduced by Dünner et al. Superclusters are identified with the ones whose mass $M > 10^{15} \, h^{-1} \, \mathrm{M_{\odot}}$, the most massive one with $M \sim 8 \times 10^{15} \, h^{-1} \, \mathrm{M_{\odot}}$, comparable to the Shapley supercluster. The spatial distribution of the superclusters remains essentially the same after the present epoch, reflecting the halting growth of the cosmic web as Λ gets to dominate the expansion of the Universe. The same trend can be seen in the stagnation of the development of the mass function of virialized haloes and bound objects. The situation is considerably different when looking at the internal evolution, quantified in terms of their shape, compactness and density profile, and substructure in terms of their multiplicity function. We find a continuing evolution from a wide range of triaxial shapes at $a = 1$ to almost perfect spherical shapes at $a = 100$. We also find a systematic trend towards a higher concentration. Meanwhile, we see their substructure gradually disappearing, as the surrounding subclumps fall in and merge to form one coherent, virialized system.

Key words: galaxies: clusters: general – Cosmology: theory – large-scale structure of Universe.

1 INTRODUCTION

The evidence for an accelerated expansion of the Universe has established the dominant presence of a 'dark energy' component. In the present cosmological paradigm, the Universe entered into an accelerating phase at $z \approx 0.7$. Observational evidence points towards a dark energy component which behaves like Einstein's cosmological constant. As long as the matter density in the Universe dominated over that of dark energy, the gravitational growth of matter concentrations resulted in the emergence of ever larger structures. Once dark energy came to dominate the dynamics of the Universe and the Universe got into accelerated expansion, structure formation came to a halt (Heath 1977; Peebles 1980). With the present-day Universe having reached this stage, the largest identifiable objects that will ever populate our Universe may be the ones that we observe in the process of formation at the present cosmological time. While no larger objects will emerge, these sufficiently overdense and bound patches will not be much affected by the global cosmic acceleration.

They will remain bound and evolve as if they are *island universes*: they turn into isolated evolving regions (Chiueh & He 2002; Busha et al. 2003; Nagamine & Loeb 2003; Dünner et al. 2006).

While clusters of galaxies are the most massive and most recently collapsed and virialized structures, the present-day superclusters are arguably the largest bound but not yet fully evolved objects in our Universe. In our accelerating Universe, we may assume they are the objects that ultimately will turn into island universes. A large range of observational studies, mostly based on optically or X-ray selected samples, show that clusters are strongly clustered and grouped together in large supercluster complexes (see e.g. Oort 1983; Bahcall 1988; Einasto et al. 1994, 2001; Quintana, Carrasco & Reisenegger 2000). These superclusters, the largest structures identifiable in the present Universe, are enormous structures comprising a few to dozens of rich clusters of galaxies, a large number of more modestly sized clumps and thousands of galaxies spread between these density concentrations.

In this study, we aim at contrasting the large-scale evolution of a structure in an accelerated Universe with that of the internal evolution of bound objects. In order to infer what will be the largest bound regions in our Universe, the *island universes*, we study the

★E-mail: p.araya@jacobs-university.de

mass function of bound objects. The abundance or mass function of superclusters serves as a good indicator of the growth of structure of a cosmological model. While large-scale structure formation comes to a halt, this will manifest itself in the asymptotic behaviour of the supercluster mass function. Meanwhile, the internal evolution of the superclusters continues as they contract and collapse into the largest virialized entities the Universe will ever contain.

We address three aspects of the continuing internal evolution of bound regions: their shape, density profile and internal substructure in terms of their cluster multiplicity. The shape of supercluster regions is one of the most sensitive probes of their evolutionary stage. We know that superclusters in the present-day Universe are mostly flattened or elongated structures, usually identified with the most prominent filaments and sheets in the galaxy distribution (e.g. Plionis, Valdarnini & Jing 1992; Sathyraprakash, Sahni & Shandarin 1998; Basilakos, Plionis & Rowan-Robinson 2001; Sheth, Sahni & Shandarin 2003; Einasto et al. 2007c). The Pisces–Perseus supercluster chain is a particularly well-known example of a strongly elongated filament (see e.g. Giovanelli, Haynes & Chincarini 1986). The distribution of shapes of bound structures is a combination of at least two factors. One is the shape of the proto-supercluster in the initial density field, and the second factor is the evolutionary state of the bound structure. We know that the gravitational collapse of cosmic overdensities – whose progenitors in the primordial density perturbation field will never be spherical (Peacock & Heavens 1985; Bardeen et al. 1986) – proceeds in a distinctly anisotropic fashion via flattened and elongated configurations towards a final, more compact triaxial virialized state (see e.g. Zeldovich 1970; Icke 1973; White & Silk 1979; Eisenstein & Loeb 1995; Bond & Myers 1996; Sathyraprakash, Sahni & Shandarin 1996; Desjacques 2008; van de Weygaert & Bond 2008).

The collapse of the superclusters will also result in a continuous sharpening of the internal mass distribution, reflected in the steepening of their density profile. While they are in the process of collapse, internal substructure of constituent clusters remains recognizable. While the subclumps merge into an ever more massive central concentration the supercluster substructure gradually fades, resulting in an increasingly uniform mass distribution. The evolving and decreasing level of substructure will be followed in terms of the evolving supercluster multiplicity function, i.e. the number of cluster-sized clumps within the supercluster region.

Representing moderate density enhancements on the scale of tens of Mpc, in the present Universe superclusters are still expanding with the Hubble flow, although at a slightly decelerated rate, or have just started contracting. Because these structures have not yet fully formed, virialized and clearly separated from each other, it is difficult to identify them unambiguously. In most studies, superclusters have been defined by more or less arbitrary criteria, mostly on the basis of a grouping and/or percolation algorithm (see e.g. Oort 1983; Bahcall 1988; Einasto et al. 1994, 2001; Quintana et al. 2000). This introduces the need for a user-specified percolation radius. Dünner et al. (2006, hereafter Paper I) attempted to define a more physically based criterion, identifying superclusters with the biggest gravitationally bound structures that will be able to form in our Universe. On the basis of this, they worked out a lower density limit for gravitationally bound structures. This limit is based on the density contrast that a spherical shell needs to enclose to remain bound to a spherically symmetric overdensity.

We use this spherical density criterion to identify bound structures in a large cosmological box. In this paper, we follow the work of Chiueh & He (2002) and Paper I. Chiueh & He (2002) numerically solved the spherical collapse model equations for self-consistent growing mode perturbations in order to obtain a theoretical criterion for the mean density enclosed in the outer gravitationally bound shell. The resulting density criterion was evaluated by Paper I on the basis of numerical simulations. They generalized it by deriving the analytical solution which also forms the basis of the current study, and in Dünner et al. (2007) extended the criterion to the limits for bound structures in a redshift space.

Various authors have addressed the future evolution of cosmic structure (Chiueh & He 2002; Busha et al. 2003; Nagamine & Loeb 2003; Dünner et al. 2007; Hoffman et al. 2007; Busha, Evrard & Adams 2007; Paper I). The internal evolution of the density and velocity structures of bound objects was followed by Busha et al. (2003), with Busha et al. (2007) focusing on the effects of the small-scale structure on the formation of dark matter haloes in two different cosmologies. Nagamine & Loeb (2003) and Hoffman et al. (2007) specifically focused on the evolution of the Local Universe. Nagamine & Loeb (2003) found that the Local Group will get detached from the rest of the Universe, and that its physical distance to other systems will increase exponentially. Hoffman et al. (2007) investigated the dependence on dark matter and dark energy by contrasting Λ cold dark matter (ΛCDM) and open cold dark matter (OCDM) models. They concluded that the evolution of structure in comoving coordinates in long term is determined mainly by the matter density rather than by the dark energy. A key point of attention in Nagamine & Loeb (2003), Hoffman et al. (2007) and Busha et al. (2007) was the mass function of objects in their simulations, on which they all agree that it hardly changes after the current cosmic epoch.

This paper is the first in a series addressing the future evolution of structure in Friedmann–Robertson–Walker (FRW) Universes. In an accompanying publication, we will specifically look at the influence of dark matter and the cosmological constant on the emerging (super)cluster population, based on the work described in Araya-Melo (2008). This study concentrates on the details of this evolution in a standard flat ΛCDM Universe.

This paper is organized as follows. In Section 2, we present a review of the spherical collapse model, including a derivation of the critical overdensity for a structure to remain bound. Section 3 describes the simulation and the group finder algorithm that we employ when determining the mass functions. This is followed in Section 4 by a qualitative description of the evolution, including a case study of the evolution of some typical bound mass clumps from the present epoch to $a = 100$. The lack of evolution in their spatial distribution in the same time interval is studied in Section 5. Section 6 presents the mass functions of the bound structures at $a = 1$ and $a = 100$ and a comparison with the ones obtained by the Press–Schechter formalism and its variants. The evolution of the shapes of the structures is studied in Section 7. In Section 8, we look into the mass distribution and density profiles. Section 9 presents the stark changes in the supercluster multiplicity function. In Section 10, its results are combined with those of the supercluster mass functions obtained in Section 6 to relate our findings to the presence and abundance of monster supercluster complexes like the Shapley and Horologium–Reticulum supercluster. Finally, in Section 11, we discuss our findings and draw conclusions on various issues addressed by our study.

2 SUPERCLUSTER COLLAPSE MODEL

The present study is based on a physical criterion for the definition of superclusters proposed by Paper I, namely that they are the largest bound (though not yet virialized) structures in the Universe.

The practical implementation of this definition suggested in that paper is through a (approximate) density threshold for regions that are gravitationally bound. Given the anisotropic nature of the collapse and the tidal influence of the cosmic surroundings (Zeldovich 1970; Icke 1973; Bond & Myers 1996; Sheth & Tormen 1999; Desjacques 2008; van de Weygaert & Bond 2008), this may only yield a rough approximation. The work by Sheth & Tormen (2002) showed that a density threshold does depend on shape and environment. One could imagine a variety of alternative physical definitions for superclusters, also relating to the assumption that they are the largest bound structures in the Universe which just have commenced to condense out of the cosmic background. One particular criterion would be to invoke the corresponding velocity field and identify them with bound regions that have turned around and started to contract, on the way towards complete collapse and virialization.

Here, we follow Paper I and assume that a global density threshold criterion, in combination with a few extra assumptions, assures a reasonably accurate identification process. This has indeed been demonstrated in the same study in a comparison of the criterion with the outcome of numerical simulations.

Paper I derive an analytical density threshold criterion for bound regions in a Universe with dark energy. We summarize this criterion and derivation in the sections below. In addition to the density threshold, we assure that a given bound region has started to materialize as a recognizable entity by including the additional requirement of the bound regions to have a virialized core. In a final step, we group the identified overlapping spherical bound supercluster objects in order to outline a region that in the observational reality would be recognized as a supercluster.

The spherical density criterion described below forms a key ingredient of our supercluster definition and for the identification procedure for singling out bound spherical regions associated with clusters (Section 3.1.5).

2.1 Spherical collapse model

The spherical collapse model (Gunn & Gott 1972; Lilje & Lahav 1991; Lahav et al. 1991) describes the evolution of a spherically symmetric mass density perturbation in an expanding Universe (also see Mota & van de Bruck 2004). Its great virtue is the ability to completely follow the non-linear evolution of a collapsing shell, as the dynamics is fully and solely determined by the (constant) mass interior to the shell. Even though the gravitational collapse of generic cosmological structures tends to be highly inhomogeneous and anisotropic, the spherical model has proven to provide a surprisingly accurate description of the more complex reality. Even in situations where it is not able to provide accurate quantitative predictions, it may be used as a good reference for interpretation of results.

We consider a flat FRW Universe with a cosmological constant Λ. The mass density parameter at the current epoch is $\Omega_{m,0}$, while $\Omega_{\Lambda,0}$ is the present value of the cosmological density parameter. The Hubble parameter at the current epoch is H_0.

A mass shell with a (physical) radius $r(t)$ at time t encloses a fixed mass M. The starting point of our derivation is the energy E per unit mass of the shell, which satisfies the equation (Peebles 1984)

$$E = \frac{1}{2}\left(\frac{dr}{dt}\right)^2 - \frac{GM}{r} - \frac{\Lambda r^2}{6} = \text{constant.} \tag{1}$$

By introducing the dimensionless variables

$$\tilde{r} = \left(\frac{\Lambda}{3GM}\right)^{\frac{1}{3}} r, \tag{2}$$

$$\tilde{t} = \left(\frac{\Lambda}{3}\right)^{\frac{1}{2}} t, \tag{3}$$

$$\tilde{E} = \left(\frac{G^2 M^2 \Lambda}{3}\right)^{-\frac{1}{3}} E. \tag{4}$$

The energy equation can be recast into the simpler dimensionless form

$$\tilde{E} = \frac{1}{2}\left(\frac{d\tilde{r}}{d\tilde{t}}\right)^2 - \frac{1}{\tilde{r}} - \frac{\tilde{r}^2}{2}. \tag{5}$$

2.2 Critical shell and turnaround radius

To delineate a bound region around a spherical mass concentration, we have to identify the critical shell. It is the shell which separates the regions that will expand forever and the ones that will at some moment in time turn around and fall in on to the core of the region.

In a Universe with a cosmological constant, the critical shell is the one that delimits the region of gravitational attraction and the region of repulsion. This translates into the radius for which the (dimensionless) potential energy $\tilde{V}$,

$$\tilde{V} = -\frac{1}{\tilde{r}} - \frac{\tilde{r}^2}{2}, \tag{6}$$

is maximized. The maximum of this potential occurs at $\tilde{r}^* = 1$. The critical shell (indicated by the subscript 'cs') is the shell with the maximum possible energy to remain attached to the spherical mass concentration,

$$\tilde{E}^* = \tilde{V}(\tilde{r}^* = 1) = -\frac{3}{2}. \tag{7}$$

The evolution of the critical shell's radius $\tilde{r}_{cs}(\tilde{t})$ can be inferred by integrating the energy equation (5) from $\tilde{t} = 0(\tilde{r} = 0)$ until epoch $\tilde{t}$, for the energy $\tilde{E} = \tilde{E}^* = -\frac{3}{2}$ of the critical shell. In a flat Universe with a cosmological constant, the vacuum energy density parameter Ω_Λ is a monotonically increasing function of the age $\tilde{t}$ of the Universe (Peebles 1980),

$$\Omega_\Lambda(\tilde{t}) \equiv \frac{\Lambda}{3H^2} = \tanh^2\left(\frac{3\tilde{t}}{2}\right). \tag{8}$$

The evolution of the critical shell $\tilde{r}_{cs}(\tilde{t})$ may therefore be expressed in terms of $\Omega_\Lambda(\tilde{t})$,

$$\Omega_\Lambda(\tilde{t}) = \left[\frac{\chi(\tilde{r}) - 1}{\chi(\tilde{r}) + 1}\right]^2, \tag{9}$$

where the variable $\chi(\tilde{r})$ is given by

$$\chi(\tilde{r}) = \left[\frac{1 + 2\tilde{r} + \sqrt{3\tilde{r}(\tilde{r} + 2)}}{1 + 2\tilde{r} - \sqrt{3\tilde{r}(\tilde{r} + 2)}}\right]^{\frac{\sqrt{3}}{2}} \times \left(1 + \tilde{r} + \sqrt{\tilde{r}(\tilde{r} + 2)}\right)^{-3}. \tag{10}$$

Evaluation of this expression shows that the critical shell radius $\tilde{r}_{cs}$ is an increasing function of Ω_Λ. The shell reaches its maximum-turnaround radius r_{max} as $\Omega_\Lambda \to 1$ and $t \to \infty$. The maximum

radius is reached when $V(\tilde{r}_{max}) = \tilde{E}^* = -\frac{3}{2}$, i.e. when

$$r_{max} = \left(\frac{3GM}{\Lambda}\right)^{1/3}, \tag{11}$$

so that the normalized radius can be interpreted as $\tilde{r} = r/r_{max}$.

For the cosmology at hand ($\Omega_{m,0} = 0.3$, $\Omega_{\Lambda,0} = 0.7$), the critical shell currently has a dimensionless radius $\tilde{r}_0 = 0.84$, i.e. it has a value of 84 per cent of its maximum radius.

2.3 Conditions for a critical shell

For the translation of the radius $\tilde{r}_{cs}$ of a bound object into a density criterion, we evaluate the average mass density $\bar{\rho}_s$ enclosed by a given shell,

$$\bar{\rho}_s = \frac{3M}{4\pi r^3}, \tag{12}$$

in terms of the critical density $\rho_c = 3H^2/8\pi G$. The shell is bound if

$$\frac{\bar{\rho}_s}{\rho_c} \geq \frac{\rho_{cs}}{\rho_c} = \frac{2\Omega_\Lambda}{\tilde{r}_{cs}^3} = 2.36. \tag{13}$$

The value 2.36 corresponds to a Universe with $\Omega_{\Lambda,0} = 0.7$. Note that for $\Omega_\Lambda = 1$ ($t \to \infty$), the critical shell's density is $\rho_{cs}/\rho_c = 2$.

The corresponding density excess δ of the spherical mass concentration with respect to the global cosmic background $\rho_u(t)(= \rho_{c,0}\,\Omega_{m,0}/a^3$, with $\rho_{c,0}$ the critical density at the present epoch) may be inferred from the expression

$$1 + \delta \equiv \frac{\rho}{\rho_u} = \frac{2\Omega_{\Lambda 0}}{\Omega_{m,0}}\left(\frac{a}{\tilde{r}}\right)^3. \tag{14}$$

On the basis of this equation, we find that a critically bound shell at the present epoch has a density excess of the order of $\delta_{cs} \approx 6.9$.

2.4 Bound object: linearly extrapolated density threshold

To be able to identify the primordial regions that correspond to bound, collapsing and/or virialized objects at any arbitrary redshift z, we need the value of the corresponding linearly extrapolated densities.

According to gravitational instability theory (Peebles 1980), in the linear regime the density excess $\delta(a)$ increases as

$$\delta(a) = D(a)\,\delta_0, \tag{15}$$

where $D(a)$ is the linear density growth factor (growing mode). In an FRW Universe with matter and a cosmological constant, it can be computed from (Heath 1977; Peebles 1980)

$$D(a) \equiv ag(a) = \frac{5\Omega_{m,0}H_0^2}{2}H(a)\int_0^a \frac{da'}{a'^3 H(a')^3}, \tag{16}$$

where $g(a)$ is the growth with respect to that in an Einstein–de Sitter Universe [$D(a)$ is normalized such that $D(a) \approx a$ for $a \to 0$].

In order to find the linear density excess δ_0 for the critically bound shell, one should evaluate its evolution at early epochs ($a \ll 1$). At these early times – when density perturbations are still very small, $\delta \ll 1$ – the linearly extrapolated density excess (equation 15) represents a good approximation for the (real) density of the object (equation 13).

Using the fact that the early Universe is very close to an Einstein–de Sitter Universe and expands accordingly, $a(t) \propto t^{2/3}$, we may infer that the early density excess δ of the bound sphere and its dimensionless radius $\tilde{r}$ is (see Appendix A)

$$\delta(t) = \frac{9}{10}\tilde{r}(t). \tag{17}$$

Using the approximate evolution of $\tilde{r}(a) \propto a$ implied by equation (14), for early times ($1 + \delta \approx 1$) we find

$$\delta(t) = \frac{9}{10}\left(\frac{2\Omega_{\Lambda,0}}{\Omega_{m,0}}\right)^{1/3} a(t). \tag{18}$$

The above equation leads us directly to the value of the linear density excess δ_0, as at the early Einstein–de Sitter phase $\delta(t) \approx a(t)\delta_0$,

$$\delta_0 = \frac{\delta}{a} = \frac{9}{10}\left(\frac{2\Omega_{\Lambda,0}}{\Omega_{m,0}}\right)^{1/3} \approx 1.504. \tag{19}$$

The corresponding linearly extrapolated density excess for marginally bound structures at the present epoch is

$$\delta_b(a = 1) = 1.17, \tag{20}$$

where we have used the approximation for $g(a) = D(a)/a$ (Carroll, Press & Turner 1992)

$$g(a) \approx \frac{5}{2}\Omega_m(a)$$
$$\times \left[\Omega_m(a)^{4/7} - \Omega_\Lambda(a) + \left(1 + \frac{\Omega_m(a)}{2}\right)\left(1 + \frac{\Omega_\Lambda(a)}{70}\right)\right]^{-1}. \tag{21}$$

These objects are due to reach turnaround at $a \to \infty$.

2.5 Tests of the spherical binding criterion

Reality is always far more complex than a simple analytical criterion is liable to cover. In addition to distinct anisotropies, internal inhomogeneities and velocity dispersions will influence the viability of the derived spherical binding criterion. By means of N-body simulations, Paper I tested the binding density criterion $\rho_{cs}/\rho_c = 2.36$ (for the current epoch) and the criterion involving the mass enclosed within the radius r_{cs}. On average, 72 per cent of the mass enclosed within r_{cs} is indeed gravitationally bound to the structure. At the same time, it was found that a mere 0.3 per cent of the mass bound to the object is not enclosed within this radius.

3 THE COMPUTER SIMULATION

We simulate a standard flat ΛCDM Universe with cosmological parameters $\Omega_{m,0} = 0.3$, $\Omega_{\Lambda,0} = 0.7$ and $h = 0.7$, where the Hubble parameter is given by $H_0 = 100\,h\,\mathrm{km\,s^{-1}\,Mpc^{-1}}$. The normalization of the power spectrum is $\sigma_8 = 1$. In order to have a large sample of bound objects, the simulation box has a side length of $500\,h^{-1}$ Mpc and contains 512^3 dark matter particles of mass $m_{dm} = 7.75 \times 10^{10}\,h^{-1}\,M_\odot$ (see Fig. 1). The initial conditions are generated at the expansion factor $a = 0.02$ (redshift $z = 49$) and evolved until $a = 100$ using the massive parallel tree N-Body/smoothed particle hydrodynamics (SPH) code GADGET-2 (Springel 2005). The Plummer-equivalent softening was set at $\epsilon_{Pl} = 20\,h^{-1}$ kpc in physical units from $a = 1/3$ to $a = 100$, while it was taken to be fixed in comoving units at a higher redshift. Given the mass resolution and the size of the box, our simulation allows us to reliably identify massive superclusters with $\sim$80 000 particles. The simulation was performed on the Beowulf cluster at the University of Groningen.

We took snapshots at five different time-steps: starting at the present time ($a = 1$), we studied the mass distribution at $a = 2$, $a = 5$, $a = 10$, to ultimately end up in the far future at $a = 100$. The latter was taken as a representative epoch at which the internal evolution of all bound objects appeared to have been completed.
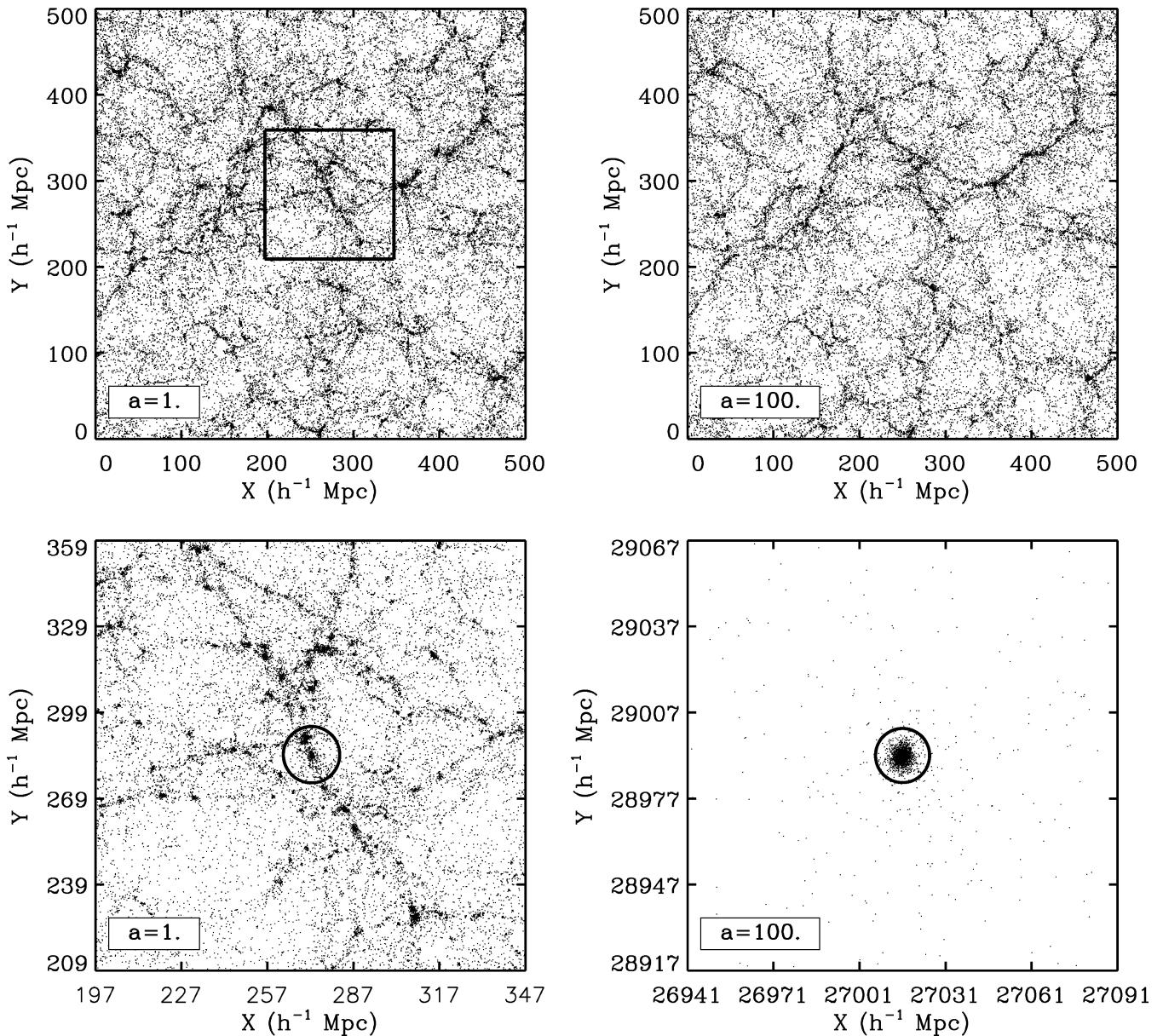
Figure 1. Simulated mass distribution at $a = 1$ (left-hand column) and $a = 100$ (right-hand column). The top panels show the particle distribution in a $500\,h^{-1}$ Mpc box, in a $30\,h^{-1}$ Mpc thick slice projected along the z-axis. Top left: mass distribution at $a = 1$. Top right: mass distribution at $a = 100$. Lower left: zoom-in on the $a = 1$ mass distribution within $50\,h^{-1}$ Mpc box indicated by the square in the top left-hand panel (similar to the $30\,h^{-1}$ Mpc thick slice along the z-direction). Lower right: region of the same $50\,h^{-1}$ Mpc *physical* size as the lower-left panel, at $a = 100$, around the same bound supercluster.

3.1 Identification of bound objects and superclusters

We identify and extract groups and objects in the simulation on the basis of a random subsample of 256^3 particles (1/8 of the total particle number). For the identification of bound structures, we apply a four-step procedure. In the first step, we find all virialized haloes in the simulations with more than 50 particles. Subsequently, we incorporate the surrounding spherical region bound to these haloes. We then join the bound spheres that overlap with each other into single bound objects. Finally, among these objects we select the most massive ones, the superclusters in the simulation volume.

3.1.1 Mass range

A first practical issue is the minimal amount of particles we deem necessary to accept a halo/object detection as significant. We choose

a minimum of 50 particles, corresponding to a mass cut of $M \geq 3.1 \times 10^{13}\,h^{-1}\,\mathrm{M_\odot}$. This means our cluster and bound object sample have an implicit bias in not containing any objects with a mass less than the mass limit. This is not a problem for the most massive objects, but may produce an incomplete sample for lower mass objects.

3.1.2 HOP and virialized halo finding

In order to find groups of particles present in our simulation, we use HOP (Eisenstein & Hut 1998). This algorithm first assigns a density estimate at every particle position by smoothing the density field with an SPH-like kernel using the n_{dens} nearest neighbours of a given particle. In our case, we use $n_{\mathrm{dens}} = 64$. Subsequently,

particles are linked by associating each particle with the densest particle from the list of its n_{hop} closest neighbours. We use $n_{hop} = 16$. The process is repeated until it reaches the particle that is its own densest neighbour.

The algorithm associates all particles with their local maxima. This procedure often causes groups to fragment. To correct this, groups are merged if the bridge between them exceeds some chosen density thresholds. Three density thresholds are defined as follows (Cohn, Bagla & White 2001):

(i) δ_{out}: the required density for a particle to be in a group.

(ii) δ_{saddle}: the minimum boundary density between two groups, so that they may have merged.

(iii) δ_{peak}: the minimum central density for a group to be independently viable.

We follow the criterion of Eisenstein & Hut (1998): δ_{outer}: δ_{saddle}: $\delta_{peak} = 1{:}2.5{:}3$. The value of δ_{peak} is associated with that of the corresponding density $\Delta_{vir}(a)$ of the virialized core of the bound regions.

3.1.3 Virial density value

To determine the value of the virial density $\Delta_{vir}(a)$ in the HOP formalism, we resort to the dynamical evolution of a spherical top-hat perturbation. The value of Δ_{vir} is obtained from the solution to the collapse of a spherical top-hat perturbation under the assumption that the object has just virialized. Its value is $\Delta_{vir} = 18\pi^2$ for an Einstein–de Sitter Universe. For the cosmology described here, at $a = 1$ its value is $\Delta_{vir}(a = 1) \approx 337$. The value at later epochs, or in other cosmologies, is obtained by solving the spherical collapse equations numerically (Gunn & Gott 1972; Lacey & Cole 1993; Eke, Cole & Frenk 1996; Kitayama & Suto 1996; Bryan & Norman 1998). An extensive description of this can be found in Araya-Melo (2008).

At $a = 100$, $\Omega_m = 4.3 \times 10^{-7}$. For this situation we resort directly to the virial theorem to determine the characteristic virial radius. According to the virial theorem, the kinetic energy K_{vir} of a body whose potential is of the form $V_{vir} = R^n$ is equal to $K_{vir} = (n/2)V_{vir}$ (Landau & Lifshitz 1960; Lahav et al. 1991). For a general case of a virialized object in a Universe with matter and a cosmological constant,

$$\tilde{K}_{vir} = -\frac{1}{2}\tilde{V}_{G,vir} + \tilde{V}_{\Lambda,vir}. \tag{22}$$

Note that here we write energies in dimensionless form (see e.g. equations 5 and 6). In this equation, $\tilde{V}_G$ is the gravitational potential energy and $\tilde{V}_\Lambda$ is the potential energy due to the cosmological constant (Lahav et al. 1991). Hence, the total energy $\tilde{E}_{vir} = \tilde{K}_{vir} + \tilde{V}_{vir}$ of a virialized object is

$$\tilde{E}_{vir} = \frac{1}{2}\tilde{V}_{G,vir} + 2\tilde{V}_{\Lambda,vir}. \tag{23}$$

Because of energy conservation, the energy at maximum expansion is equal to the energy at virialization. This translates into the following equation for the dimensionless radius:

$$\tilde{r}^2 + \frac{1}{2\tilde{r}} = \frac{3}{2}. \tag{24}$$

This is a cubic equation with solutions $\tilde{r} \approx -1.366$, $\tilde{r} = 1$ and $\tilde{r} \approx 0.366$. The first is an unphysical solution. The solution $\tilde{r} = 1$ is the maximum radius of the critically bound shell (see equation 2.3). The third value, $\tilde{r} \approx 0.366$, is the virial radius of the enclosed mass M. The corresponding virial density excess of the mass clump would be $1 + \Delta_{vir} = \bar{\rho}/\rho_c \approx 40.8$.

3.1.4 Clusters

Besides the definition of a sample of superclusters, we also identify the clusters in our simulation. Their identity is more straightforward to define, since we may presume they are virialized.

Virialized haloes, as identified by HOP (Section 3.1.2), with masses larger than $3 \times 10^{13}\, h^{-1}\, M_\odot$, are considered as *clusters*. Note that, by definition, these clusters are identical to the bound object cores produced in step 1 of our supercluster finding procedure (Section 3.1.2).

3.1.5 Bound halo identification

Once we have identified the virialized haloes in our sample, we have to proceed by outlining the gravitationally bound region around these cores and, if necessary, join them together into a supercluster. In practice, we do this as follows.

Of an identified HOP halo, we take the location of the densest particle as a first estimate of the centre of mass. Subsequently, we grow a sphere around this centre, with the radius being increased until the mean overdensity within the corresponding radius reaches a value of $300\rho_c$. This value is chosen in order to find the densest core of the structure. We then calculate the centre of mass of this sphere and repeat the process, iterating until the shift in the centre between successive iterations is less than 1 per cent of the radius.

With the final centre of mass, we apply the criterion of equation (13) for identifying the bound spherical region around the HOP core. To this end, we determine the radius r_{cs} at which the average interior density ρ_{cs}/ρ_c reaches a value $\rho_{cs}/\rho_c = 2.36$ at $a = 1$, 2.22 at $a = 2$, 2.06 at $a = 5$, 2.02 at $a = 10$ and 2.00 at $a = 100$ (see Section 2.3).

### 3.1.6 Joining haloes: bound objects

The procedure outlined in the previous paragraph will frequently lead to overlapping bound spheres that in reality will be bound to each other. In order to account for this, we follow a radical prescription. If two spheres overlap, we proceed with the most massive one and join the lower mass sphere to the high-mass one while removing it from the list of objects.

We found that by following this procedure at $a = 100$, such overlaps do not occur. It implies that in the far future nearly all bound objects are compact and isolated islands in the Universe. At much earlier epochs, and specifically at $a = 1$, it does turn out to occur for a significant fraction of the bound spheres.

3.1.7 Superclusters and bound objects

Because not all bound objects would be prominent enough to be a supercluster, we use a mass threshold to select the superclusters among the bound objects in our sample. The mass threshold is chosen to be $M_{sc} = 10^{15}\, h^{-1}\, M_\odot$, approximately the mass of the Local Supercluster. Although this value is somewhat arbitrary, and a somewhat different value might also have been viable, it represents a reasonable order of magnitude estimate.

As a result, we reserve the name *bound objects* for all the objects that have ended up in our sample, while *superclusters* are the subset with masses higher than our supercluster mass threshold of $10^{15}\, M_\odot$.
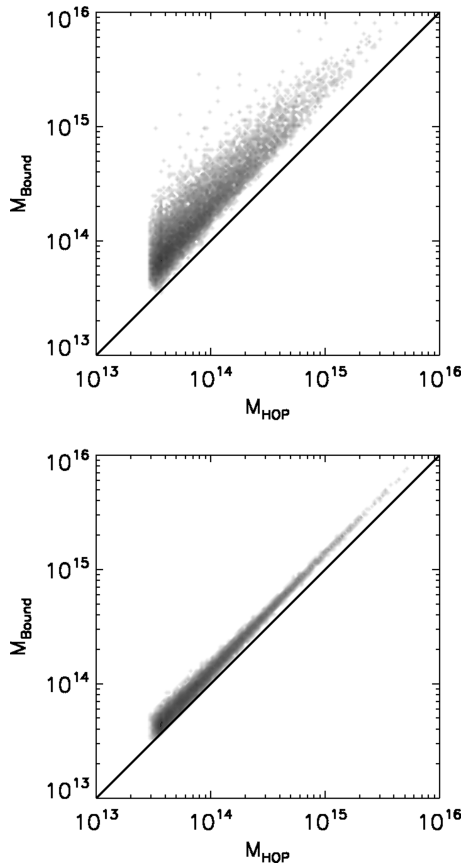
Figure 2. Scatter plots of the mass of identified bound objects, M_{bound}, against the mass of the virialized HOP halo that forms its core, M_{HOP}. The density of points (M_{HOP}, M_{Bound}) in the scatter diagram is depicted in terms of an isodensity contour map. The highest concentration of points has the darkest (black) shade, gradually fading towards light colours. Top: $a = 1$. Bottom: $a = 100$.

3.1.8 Sample completeness

Fig. 2 helps us to evaluate the completeness of our object sample. The panels contain scatter plots of the total mass of the bound objects versus the HOP mass of their corresponding virialized cores.

Evidently, the lower-right region is empty: HOP groups will always be less massive than the bound groups. There is a correlation between both masses, but with a high scatter. As expected, the evolution of bound objects towards fully virialized clumps expresses itself in a substantially stronger correlation at $a = 100$ than at $a = 1$. On the basis of these relations, we may conclude that at $a = 1$ the sample is complete for masses greater than $2 \times 10^{14} \, h^{-1} \, \text{M}_{\odot}$, while at $a = 100$ the sample is complete for masses down to $6 \times 10^{13} \, h^{-1} \, \text{M}_{\odot}$. In order to keep the samples comparable, we use a mass completeness threshold of $2 \times 10^{14} \, h^{-1} \, \text{M}_{\odot}$ at $a = 1$ and $1.4 \times 10^{14} \, h^{-1} \, \text{M}_{\odot}$ at $a = 100$ (see discussion in Section 6).

3.1.9 The object sample

At $a = 1$ HOP finds ~20 600 virialized 'clusters' with more than 50 particles, i.e. haloes with a total mass $M \geq 3.1 \times 10^{13} \, h^{-1} \, \text{M}_{\odot}$. At $a = 100$ it finds ~18 000 virialized objects. These will be taken as the starting point for our supercluster finding procedure. They also constitute the cluster sample in our simulation.

After determining the connected bound region and joining these overlapping bound spheres (see Section 3.1.6), plus checking for sample completeness, we finally end up with a sample of ~4900 bound objects at the current epoch. At the other epochs, from $a = 2$ to $a = 100$, this is approximately the same number. Of these, ~535 are superclusters (at $a = 1$), while 17 are truly massive supercluster complexes with $M_{\text{sc}} > 5 \times 10^{15} \, h^{-1} \, \text{M}_{\odot}$.

4 EVOLUTION OF BOUND OBJECTS

The two top panels of Fig. 1 show a slice of 30 h^{-1} Mpc width of the particle distribution projected along the z-axis, at $a = 1$ and $a = 100$. By taking a region of the same physical size at both epochs, the effect of the de Sitter expansion of the Universe becomes manifestly clear.

At $a = 1$, the large-scale structure of the cosmic web is well established and its morphology and character hardly change thereafter. The lower-left panel zooms in on the square region of the top-left panel. Centred on a massive structure, it shows the mass distribution at $a = 1$. The radius of the circle is that of the bound region, according to the criterion of equation (13). It shows that it is well connected with the surrounding structure. The same object, but now at $a = 100$, is depicted in the lower-right panel (with the same *physical scale*). We see that the size of the bound object is nearly the same at both expansion factors. While in comoving coordinates the accelerated expansion of the Universe results in a freezing of structure growth on scales much larger than the initial size of superclusters, in physical coordinates the separation of structures continues and grows exponentially in time. This results in clearly detached regions which evolve in complete isolation: genuine *cosmic islands*.

4.1 Case studies

To get an impression of the internal and external evolution of the bound objects in our simulation, we focus on a few specific objects. By following qualitatively the 'internal' evolution of three bound objects, we intend to set the scene for the further analysis in this study.

Fig. 3 displays the evolution of one of the most massive objects in our sample. At $a = 1$, it has a substantial degree of substructure (Fig. 4, left-hand side). The centre of the supercluster is dominated by the massive central cluster that is the virialized object from which we constructed the remainder of the supercluster. It forms the centre of a huge complex, connecting the surrounding matter distribution via prominent filamentary extensions. These form the transport channels along which mass flows into the central supercluster region. Noteworthy is the large number and variety of subclumps along the filaments and around the centre of the supercluster. This high-mass supercluster undergoes a radical change towards the future.

By $a = 2$ we see that most of the surrounding material has fallen into the central core, with a dramatic decrease in the number of surrounding subclumps. While at $a = 5$ we still see a significant number of small clumps around the central supercluster, by $a = 10$ only a few individuals seem to have survived. Comparing the first and second panels with the panels corresponding to $a = 5$ and $a = 10$ also seems to suggest that the infalling subclumps at later epochs have a lower mass.

With respect to the morphological character of the surrounding mass distribution, we note that at $a = 2$ we can still discern the
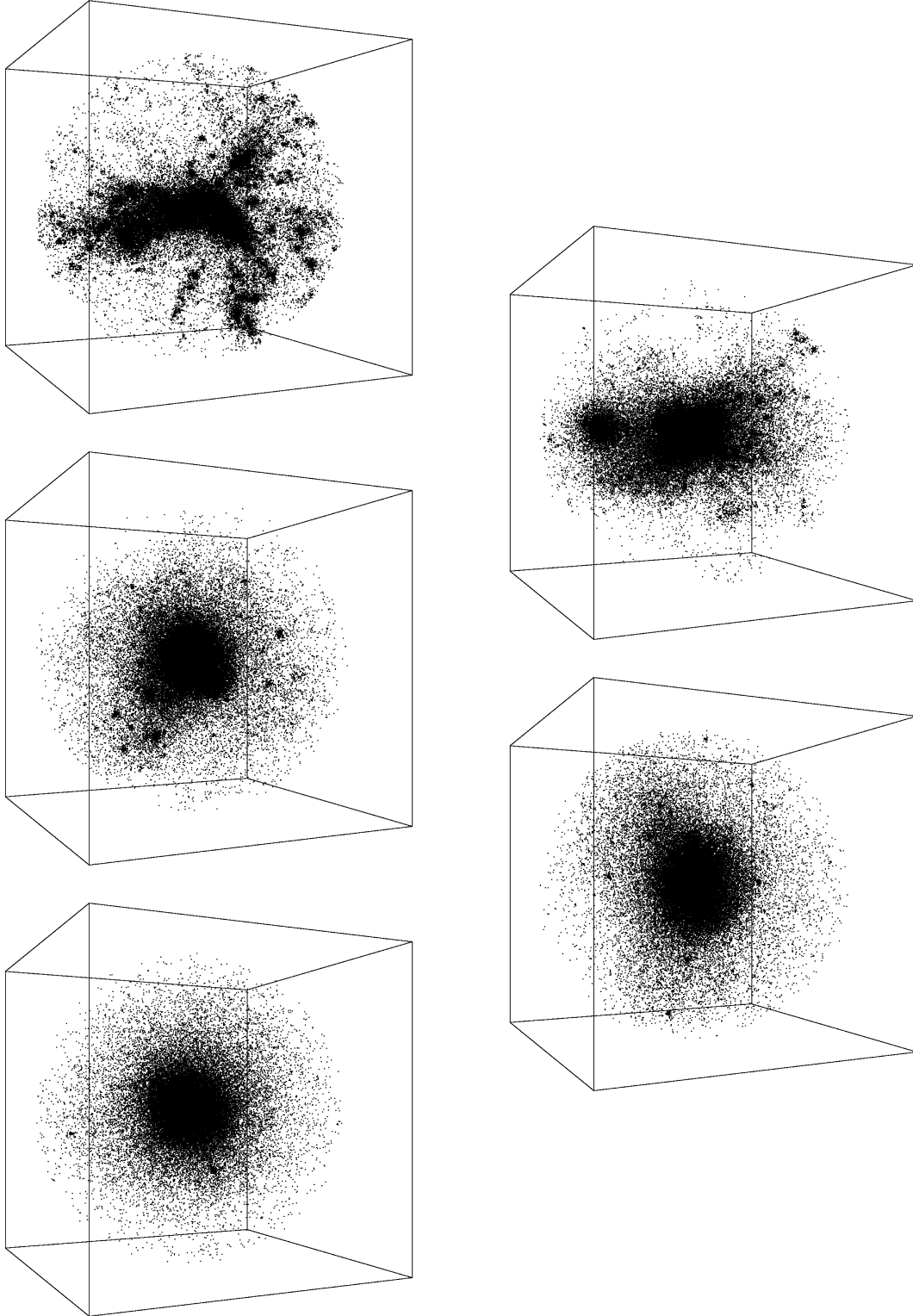
Figure 3. Evolution of one of the most massive objects in our simulation, with a present-day mass of $M \sim 6.8 \times 10^{15} \, h^{-1} \, \mathrm{M_\odot}$, at $a = 1$. The supercluster is shown at $a = 1, a = 2, a = 5, a = 10$ and $a = 100$ (zigzagging from top left to bottom left). The size of the box is always $14 \, h^{-1}$ Mpc in physical coordinates.

vague remnants of the salient filamentary patterns at the present epoch. Nonetheless, most of the formerly richly patterned web-like structure has disappeared and seems to have resolved itself as its mass accreted on to the supercluster. The supercluster has also assumed a more smooth and roundish appearance, even though at $a = 2$ we can still recognize the original geometry, in terms of both its elongated shape and its orientation along the same direction. At even later epochs, the trend towards a highly centralized and regular mass concentration with a nearly perfect spherical shape continues inexorably. At $a = 10$ we may still just recognize some faint matter
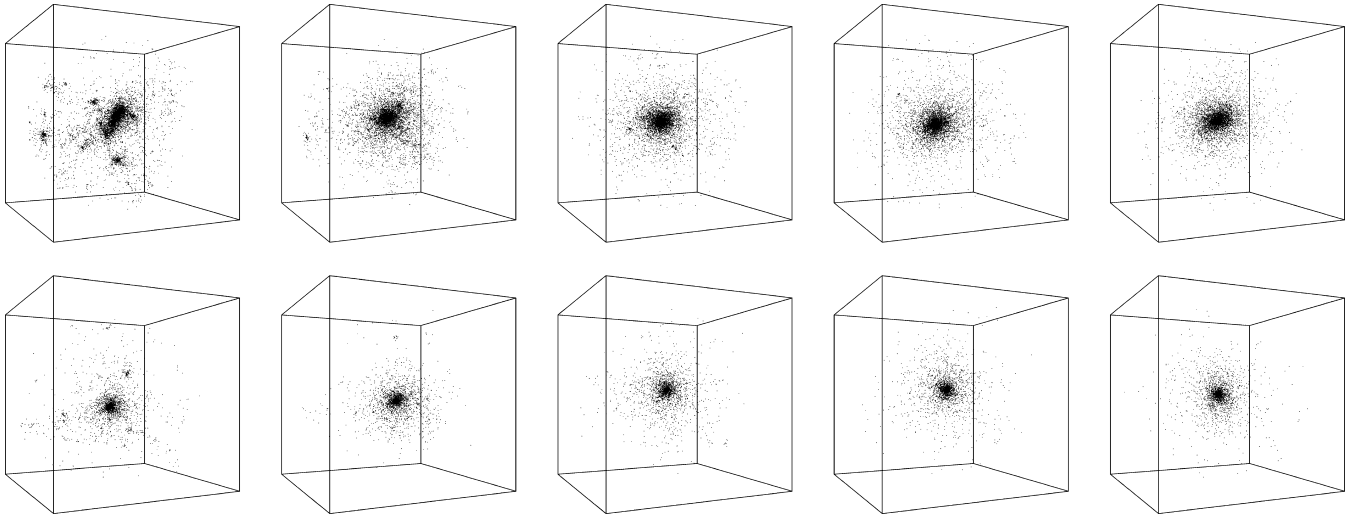
Figure 4. Evolution of two different bound objects in the simulation. Each row shows the evolution of a single object at $a = 1, a = 2, a = 5, a = 10$ and $a = 100$. The particle positions are in physical coordinates. The box sizes have been scaled to the size of the mass concentrations and therefore differ among each other. Top row: intermediate mass bound object, $M \sim 5.6 \times 10^{14} \, h^{-1} \, \mathrm{M}_{\odot}$ ($a = 1$). Box size is $6 \, h^{-1}$ Mpc . Bottom row: least massive bound object, with a present-day mass of $\sim 2 \times 10^{14} \, h^{-1} \, \mathrm{M}_{\odot}$ (box size at $a = 1$: $4 \, h^{-1}$ Mpc, box size at $a = 100$: $3 \, h^{-1}$ Mpc). The evolution of these medium and low-mass objects should be compared to that of the massive supercluster in Fig. 3.

extensions at the edge of the supercluster. However, these do no longer bear the mark of its original orientation and shape. At the final time-step, $a = 100$, the object has reached the ultimate configuration of a perfectly regular, nearly spherical and centrally concentrated and largely virialized dark matter halo. All surrounding substructure within the binding radius has fallen and has been entirely absorbed while the supercluster attained a perfectly virialized configuration: the big mass concentration has become a true island universe.

The evolution of the massive supercluster is compared with that of two more moderate bound mass clumps in Fig. 4. The top row shows the evolution of a medium mass bound object, with a mass of $M \sim 5.6 \times 10^{14} \, h^{-1} \, \mathrm{M}_{\odot}$ (at $a = 1$), while the bottom row depicts the development of the least massive bound object. The present-day mass of the latter is $M \sim 2 \times 10^{14} \, h^{-1} \, \mathrm{M}_{\odot}$. Even though the medium mass object (central row) shares a similar trend towards a centrally concentrated virialized clump, we also notice that its influence over the surroundings is considerably less pronounced and extends over a considerably smaller region. At $a = 1$ we recognize some relatively large subclumps in its surroundings, most of which by $a = 2$ have fallen in. The subclumps and the more diffusely distributed surrounding matter do not seem to display a pronounced spatial pattern and they do not appear to be organized in web-like filamentary extensions. Even though to some extent this may be a consequence of the limited resolution of our simulation, it undoubtedly pertains also to the substantially lower dynamical (tidal) influence of the clump over its surroundings (see e.g. Bond, Kofman & Pogosyan 1996). After $a \approx 2$–3, the infall of matter proceeds mostly through quiescent accretion, resulting in a gradual contraction of the object into a moderately elongated ellipsoidal halo.

Even less outstanding is the evolution of the low-mass bound object (bottom row). It hardly shows any substructure and seems to consist only of a central region and a few particles within the binding radius. Between an expansion factor of $a = 2$ and $a = 100$ the changes in appearance are only marginal in comparison to those seen in the more massive bound structures.

5 THE SPATIAL DISTRIBUTION OF BOUND OBJECTS AND SUPERCLUSTERS

The evolving spatial distribution of the bound objects in our simulation is shown in Fig. 5. From this direct visual inspection, we see that the spatial distribution of the bound structures hardly changes between $a = 1$ and $a = 100$.

Immediately striking is the fact that the bound object or supercluster 'filling factor' f dramatically declines as time proceeds. Defining the filling factor as the fractional volume occupied by bound objects and superclusters,

$$f \equiv \sum_{j} V_j / V_{\text{box}}, \qquad (25)$$

we may appreciate the strength of the effect by inspecting Table 1. At the onset, i.e. the present time, the bound objects and superclusters take up a sizeable fraction of the cosmic volume: $\sim$3.3 per cent for the bound objects and $\sim$1.2 per cent in the case of the superclusters. Even while towards later times the number of bound objects with virialized cores is increasing (unlike that for the superclusters), the volume fraction is rapidly declining. After $a = 10$ they occupy a negligible fraction of the Universe, superclusters only a fractional volume in the order of $\sim 10^{-8}$. The tremendous exponential expansion of the Universe as a result of the cosmological constant clearly renders each bound cluster and supercluster an ever more isolated and lonely island in the Universe!

The other important observation is that the spatial distribution of bound clumps hardly changes from $a = 1$ to $a = 100$. The spatial patterns visible in the object distribution at $a = 1$ are very similar to the ones at a much later epoch. Clustering does not seem to get any more pronounced after the present epoch $a = 1$.

5.1 Correlation analysis

To quantify the visual impression of the spatial distribution of bound objects and superclusters in our sample, we have determined their
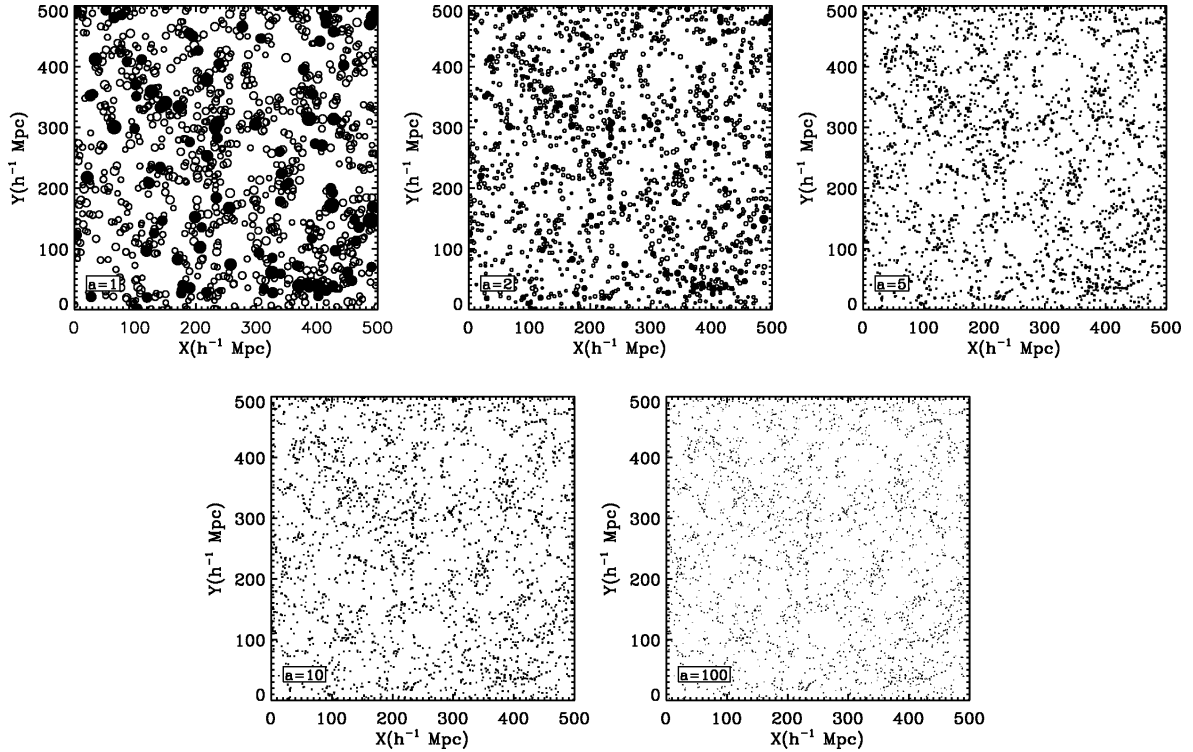
Figure 5. Spatial distribution of bound structures at five different expansion factors: $a = 1$ (top-left panel), $a = 2$ (top-centre panel), $a = 5$ (top-right panel), $a = 10$ (bottom-left panel) and $a = 100$ (bottom-right panel). The panels show the distribution in comoving coordinates in a $100\,h^{1-}$ Mpc thick slice projected along the z-axis. The bound structures are presented as circles with a size equal to their comoving radius (note that the comoving size of the bound objects shrinks as the Universe evolves into the future). Among the bound objects, the dark circles indicate the superclusters ($M \geq 10^{15}\,h^{-1}\,\mathrm{M_\odot}$).

Table 1. Filling factor of bound objects (left) and superclusters (right) at five expansion factors: $a = 1$, $a = 2$, $a = 5$, $a = 10$ and $a = 100$.

	Bound structures	Superclusters
$a = 1$	3.34×10^{-2}	1.24×10^{-2}
$a = 2$	4.34×10^{-3}	1.37×10^{-3}
$a = 5$	3.31×10^{-4}	8.64×10^{-5}
$a = 10$	4.24×10^{-5}	1.01×10^{-5}
$a = 100$	4.14×10^{-8}	0.91×10^{-8}

spatial two-point correlation function $\xi(r)$ (see e.g. Peebles 1980) at different epochs.

The left-hand frame of Fig. 6 presents the two-point correlation function $\xi(r)$ at $a = 100$ for three different samples: the complete simulation sample of bound objects, the subset of bound objects with mass $M > 10^{14}\,\mathrm{M_\odot}$ and the superclusters. We assess $\xi(r)$ in terms of comoving distances, in physical coordinates one should evidently take into account the dilution factor due to the expansion of the Universe. In our correlation analysis we take $a = 100$ as the reference point, as we will see that the situation at other epochs is more or less comparable. In all three cases, we observe the strong clustering of the populations. Over a large range, almost extending out to a distance of $r \approx 100\,h^{-1}$ Mpc, the bound objects and superclusters do show a significant level of clustering. This can be inferred from the inspection of the lin–lin plot of $\xi(r)$ in the inset in Fig. 6 (left-hand frame).

To first approximation, $\xi(r)$ behaves like a power-law function,

$$\xi(r) = \left(\frac{r_0}{r}\right)^{\gamma}. \tag{26}$$

This is particularly evident for the sample of superclusters, which at $a = 100$ has a correlation length $r_0 = 23 \pm 5\,h^{-1}$ Mpc and a slope $\gamma \approx 2.1 \pm 0.1$. Within the error bounds, the numbers at the other time-steps are equivalent. While the overall behaviour of the correlation function of all bound objects, or that of the ones with $M > 10^{14}\,\mathrm{M_\odot}$, does resemble that of a power law, we also find marked deviations. At the small distances where the clustering is strongest, $r < 5\,h^{-1}$ Mpc, we find that $\xi(r)$ has a distinctly lower slope, $\gamma \approx 1.4$–1.5. In the large-scale regime, i.e. beyond the clustering length $r_0 \approx 11.5\,h^{-1}$ Mpc, the slope steepens considerably and attains a value close to $\gamma \approx 2.0$ at $a = 100$.

We find that more massive objects are more strongly clustered, confirming the impression obtained from Fig. 5 (see e.g. top-left frame). Comparison between the clustering of the whole sample with that of the subsample of objects with mass $M > 10^{14}\,\mathrm{M_\odot}$, and in particular that of superclusters, shows that the more massive samples have a stronger correlation function over the whole range of distances. In addition, we may also observe that the clustering of superclusters seems to extend out to larger distances than that of all objects. That is, for superclusters $\xi(r) > 0$ out to distances larger than $r \approx 100\,h^{-1}$ Mpc.

This clustering scaling behaviour is a telling illustration of the (clustering) bias of more massive objects with respect to the global average, and has to some extent be related to the properties of the peaks in the Gaussian primordial density field (Kaiser 1984). Our findings relate directly to the known clustering behaviour of clusters. Since Bahcall & Soneira (1988) found that the clustering strength of clusters is an increasing function of the cluster richness, a large variety of studies have uncovered the systematics of this clustering bias (see e.g. Szalay & Schramm 1985; Peacock & West 1992; Einasto et al. 2002). Particularly enticing are the recent results
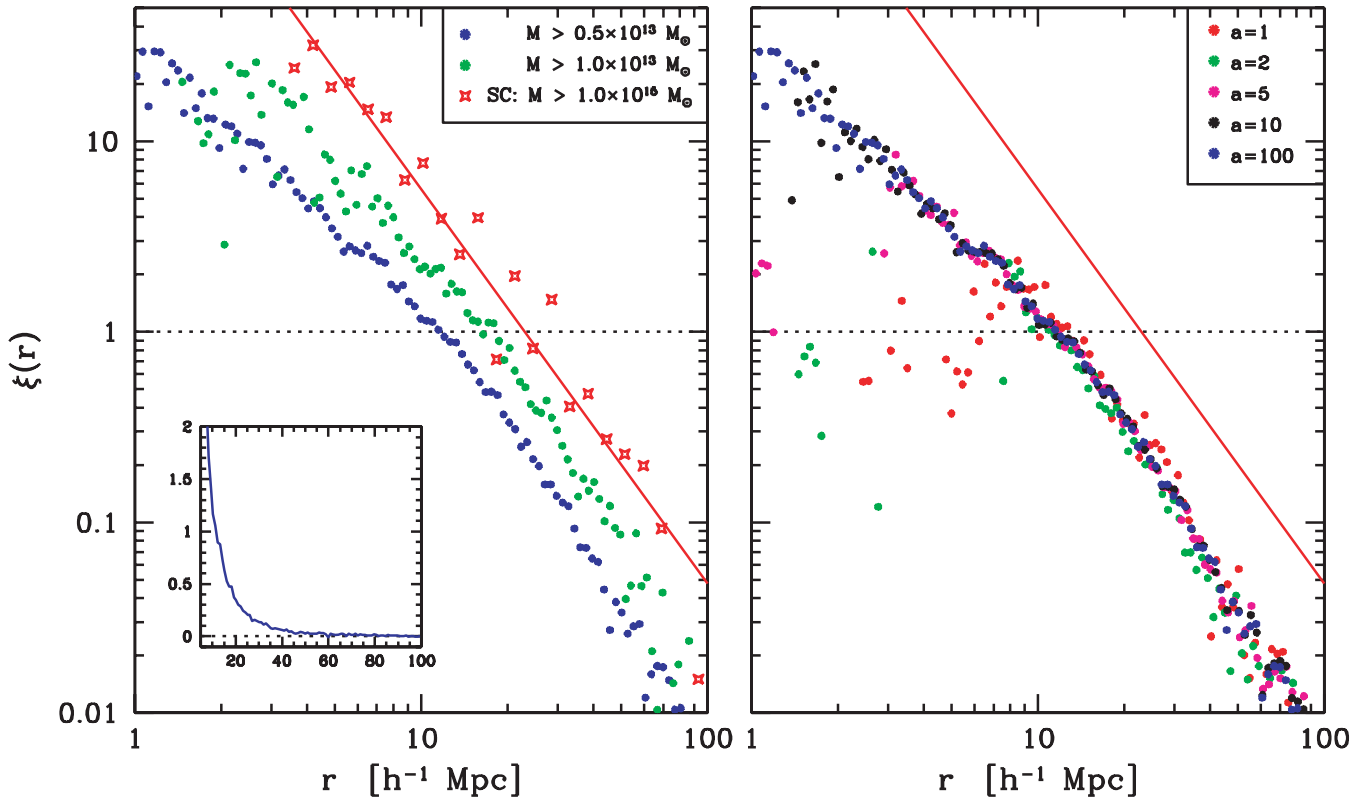
Figure 6. Two-point correlation function $\xi(r)$ of bound objects and of superclusters. The correlation function is shown in a log–log plot. Left: two-point correlation function at $a = 100$ for three different samples: all bound objects in the simulation sample (blue dots), bound objects with mass $M > 10^{14}$ M$_\odot$ (green dots) and superclusters (red stars). The red line is a power-law fit to $\xi(r)$ of the superclusters. The inset is the lin–lin plot of $\xi(r)$ for the whole object sample. Right: the evolution of $\xi(r)$. The two-point correlation function of the whole object sample at five different epochs, $a = 1, 2, 5, 10$ and 100. The corresponding colours are indicated at the top-right corner of the frame. For guidance the red line shows the power-law fit to the supercluster $\xi(r)$ at $a = 100$.

obtained for cluster samples extracted from the Sloan Digital Sky Survey (SDSS) survey (Bahcall et al. 2003; Estrada, Sefusatti & Frieman 2009).

In the right-hand frame of Fig. 6, we assess the evolution of the two-point correlation function of the complete sample of bound objects, from $a = 1$ to $a = 100$. With the exception of some evolution at short distances, $r < 5 \, h^{-1}$ Mpc, there is no significant evolution of the two-point correlation function over the full range of distances. This is a manifest illustration of the stagnation of structure evolution in an accelerating Universe on scales larger than several Megaparsec. The situation appears to be exactly the same for the stronger correlation function of superclusters: from $a = 1$ to $a = 100$ superclusters keep the same level of clustering. Of course, this is a clear manifestation of the expected end of structure growth after the Universe went into acceleration at $z \approx 0.7$. Note that for reasons of clarity, in the right-hand frame of Fig. 6 we restrict ourselves to merely plotting the power-law fit to the supercluster correlation function.

6　GLOBAL EVOLUTION: MASS FUNCTIONS

With the identification of superclusters, we may ask how much mass is contained in them at the present epoch and at $a = 100$. At $a = 1$, the entire sample of bound objects in our simulation box amounts to $2.73 \times 10^{18} \, h^{-1}$ M$_\odot$. At $a = 100$ this has grown to a total mass of $2.83 \times 10^{18} \, h^{-1}$ M$_\odot$. This represents 26 per cent, respectively 27 per cent, of the total mass in our simulated Universe ($1.04 \times 10^{19} \, h^{-1}$ M$_\odot$).

We may make two immediate observations. First, given that bound objects tend to lose around 28 per cent of their mass towards $a = 100$ (see below), it must mean that the number of bound objects fulfilling our criterion – of containing one or more virialized cores – is still growing from $a = 1$ towards $a = 100$. It may also indicate a problem in applying a purely spherical density criterion: at $a = 1$ mass concentrations are more aspherical and inhomogeneous, while at $a = 100$ they are nearly spherical concentrated mass concentrations (see Section 7). Perhaps even more tantalizing is the fact that apparently more than 70 per cent of mass in the Universe will remain outside of the supercluster islands and will keep on floating as a lonely population of low-mass objects in a vast cosmic void.

Perhaps the most outstanding repercussion of the slowdown of large-scale structure formation in hierarchical cosmological scenarios is the fact that the condensation of new objects out of the density field will gradually come to a halt. This should be reflected in the mass spectrum of the objects that were just on the verge of formation around the time of the cosmological transition. Here, we investigate the mass distribution of superclusters, i.e. bound but not yet fully virialized structures. For comparison we also investigate a sample of virialized haloes.

6.1　Theoretical mass functions

Fig. 7 shows the evolution of the mass function of virialized objects predicted by the Press–Schechter formalism (Press & Schechter 1974) and the Sheth–Tormen excursion set prescription (Sheth & Tormen 1999) for the current cosmology.
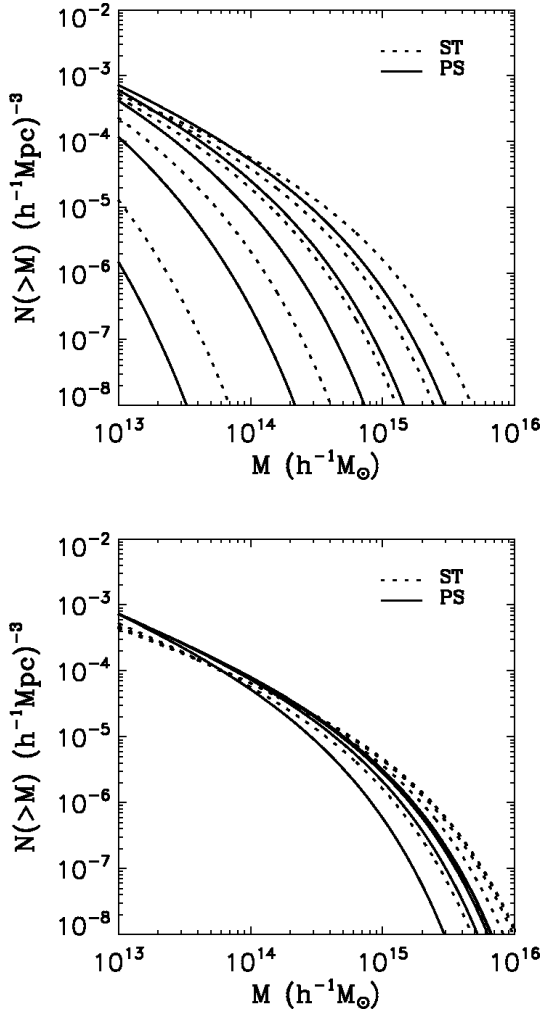
Figure 7. Theoretical mass functions for virialized objects in a ΛCDM Universe ($\Omega_{m,0} = 0.3$, $\Omega_{\Lambda,0} = 0.7$, $h = 0.7$). Shown are the Press–Schechter mass functions (dashed lines) and the Sheth–Tormen mass functions (solid lines). Top: the mass functions at redshifts $z = 4, 2, 1, 0.5$ and 0 (from left to right). Bottom: the mass functions at expansion factors $a = 1, 2, 4, 10$ and 100 (from left to right).

The Sheth–Tormen expression takes into account the anisotropic collapse of dark haloes. We also compare our mass functions to the heuristic simulation-based mass function suggested by Jenkins et al. (2001). We refer to Appendix B for a listing of the expressions for these mass functions.

The top panel shows the strong evolution in the past, by depicting the mass functions at $z = 4, 2, 1, 0.5$ and 0. It shows that structure grows in mass and number while the Universe expands. The future evolution is a lot less strong, as evidenced by the mass functions at expansion factors $a = 1, 2, 4, 10$ and 100 in the bottom panel. After $a = 1$ the number of low-mass objects does not change substantially, while after $a = 4$ evolution comes to a complete halt. This may be best appreciated from the fact that the curves for $a = 10$ and $a = 100$ overlap completely.

We see that the Sheth–Tormen approximation predicts a higher number of massive clusters than the Press–Schechter formalism. As anisotropic collapse speeds up the contraction along the minor axis of an object, there is a higher number of regions reaching a sufficiently large overdensity before dark energy prevents any

further evolution. Implicitly, this lowers the number of low-mass objects as more get absorbed into the high-mass superclusters.

6.2 Simulation mass functions

We assess the mass function of the virialized haloes, the objects identified by HOP on the basis of the prescription in Section 3.1.2, and that of the bound (supercluster) objects that were identified according to the criterion specified in Section 3.1. Given that we do not expect a radical change in mass functions between the present epoch and $a = 100$, we restrict the comparison to the simulation mass functions at $a = 1$ and $a = 100$.

Fig. 8 shows the mass functions of the virialized haloes found by HOP (left-hand panel) and of the bound objects (central panel) at $a = 1$ and $a = 100$. As expected, the number of massive virialized haloes increases as we go from $a = 1$ to $a = 100$. The increase is only minor, yet significant, and a manifestation of the freezing of structure formation (see also Nagamine & Loeb 2003). The mass functions at $a = 1$ and $a = 100$ also reflect the continuing hierarchical evolution within the realm of the bound supercluster regions. There is a definitive increase in the number of the most massive clumps, going along with a decrease at the low-mass side of the mass function.

When turning towards the mass function for the bound (supercluster) regions (central panel), we find the same mass function at $a = 1$ and $a = 100$, except for a slight decrease in the mass of the objects over the whole mass range. There is a loss of mass, amounting to some 28 ± 13 per cent of the mass enclosed within the critical radius of the superclusters at $a = 1$ (Paper I). This is substantially more than the mere 1 per cent mass gain as a result of accretion of mass in between $a = 1$ and $a = 100$. The loss of mass has to be ascribed to the virialization process of, and within, the bound object. A major factor in this is the abundant substructure in the supercluster at the present epoch as opposed to the smoothened mass distribution within the ultimate supercluster island at $a = 100$. In order to correct for this 'reduced' mass we renormalize the supercluster mass function into a *reduced* supercluster mass function, simply by multiplying the masses by a factor of 0.72. As may be observed in the right-hand panel of Fig. 8, we find an almost perfect overlap between the mass function at $a = 100$ and its reduced equivalent at $a = 1$.

6.3 Comparison of simulated and theoretical mass functions

Fig. 9 shows the cumulative mass function of the virialized objects found by HOP at $a = 1$ and at $a = 100$, and compares them with three theoretical mass functions (see Appendix B).

6.3.1 Mass functions of bound objects and superclusters

To compare the mass function of the bound (supercluster) regions with the theoretical Press–Schechter and Sheth–Tormen functions we need to specify a critical overdensity corresponding to the bound (supercluster) regions in our sample (see Appendix B). Because in this study these are assembled on the presumption that they are marginally bound, we use the corresponding value of the linear extrapolated density excess, $\delta_b = 1.17$, derived in Section 2.4 (see equation 20).

At $a = 1$, the Sheth–Tormen function seems to provide a better fit than the Press–Schechter function to the bound object mass spectrum, in particular for the tail of massive superclusters. It demonstrates the importance of morphological and tidal influences on the mass spectrum of these generically non-spherical objects (see
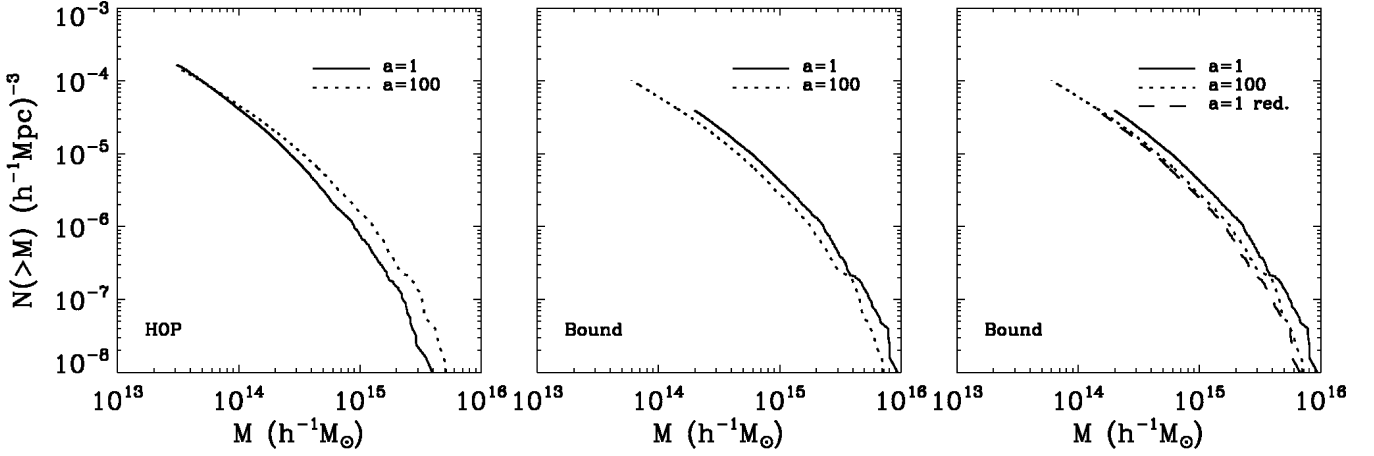
Figure 8. Mass functions of virialized haloes and of bound objects. Left: integrated mass function $N(>M)$ for virialized HOP objects in the simulation, at $a = 1$ (solid line) and $a = 100$ (dotted line). Centre: integrated mass function $N(>M)$ for bound objects in the simulation, at $a = 1$ (solid line) and $a = 100$ (dotted line). Right: the integrated mass function $N(>M)$ for bound objects compared with the *reduced* $a = 1$ mass function (dashed line). See text for explanation.

Section 7). At $a = 100$ the Press–Schechter function provides a substantially better fit to the bound object mass function. This may be related to the fact that the Press-Schechter (PS) formalism implicitly assumes pure spherical collapse, which we will see in Section 7 agrees quite well with the shape of superclusters at $a = 100$. Also, we find that in the far future, when most of our superclusters have become isolated and largely virialized islands, it is appropriate to compare with a Press–Schechter or Sheth–Tormen mass function based on another critical density value. In between $a = 1$ and $a = 100$ most *cosmic islands* will reside in a dynamical phase somewhere between marginally bound and full collapse, implying a critical value in between $\delta_b = 1.17$ (equation 20) and the collapse threshold $\delta_c = 1.675$ (equation B4).

It is also clear that the Jenkins function does not provide a suitable fit to the supercluster mass function. This may not be surprising given the fact that it is a numerical approximation of the mass function of collapsed and virialized haloes in N-body simulations and as such does not explicitly include an adjustable density threshold δ_c.

6.3.2 Cluster mass function

It is more straightforward to compare the mass function of the clusters, or HOP haloes, in our simulation with that of the three theoretical mass functions for virialized objects. For these fits we use the critical collapse density value $\delta_c = 1.675$, the value for our cosmology according to equation B4. The Jenkins approximation is of course independent of the value of δ_c.

At $a = 1$, the Jenkins mass function (Jenkins et al. 2001) is the one that fits best (dot–dashed line), which is perhaps not entirely surprising given its N-body simulation background. The Press–Schechter mass function represents a good fit at the lower mass end, although it underestimates the number of high-mass clusters. Governato et al. (1999) claim that a critical density value $\delta_c = 1.775$ would provide a better fit, and indeed it would lead to a small, yet significant, improvement of the Sheth–Tormen mass function.

For $a = 100$ we adjust the parameters of the Jenkins function, using the fitting parameters for $\Omega_m = 0$ listed in Evrard et al. (2002). With these parameters, it agrees very well with the HOP mass function, although it slightly overestimates the number of lower
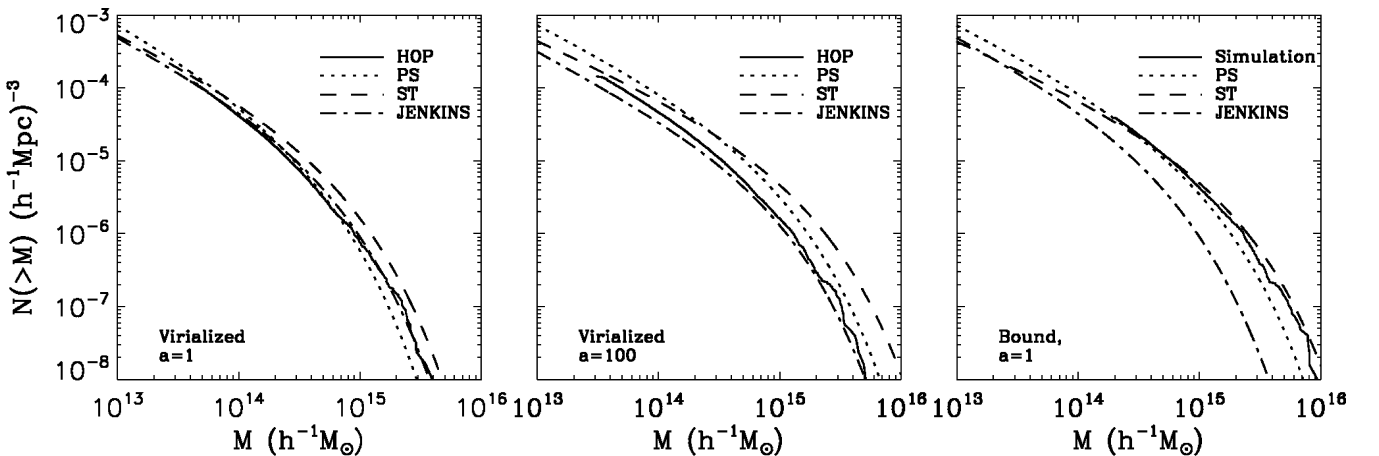
Figure 9. Mass functions of virialized haloes and of bound objects compared with three theoretical mass functions. These are the Press–Schechter mass function (dotted line), the Sheth–Tormen function (dashed line) and the Jenkins function (dot–dashed line). For the virialized HOP haloes, the critical overdensity δ_c for the PS and ST functions is the one for collapse, for the bound objects the value δ_b for assuring a bound object (Paper I; this study). Left-hand panel: the $a = 1$ integrated mass function $N(>M)$ of HOP haloes. Centre: the $a = 100$ integrated mass function $N(>M)$ of HOP haloes. Right-hand panel: the $a = 100$ integrated mass function $N(>M)$ of bound objects.

mass objects. However, for Jenkins' original parameter values, it would lead to a significant overabundance of objects with respect to the ones found in the simulations.

Neither the pure Press–Schechter nor the Sheth–Tormen function manages to fit the mass spectrum at $a = 100$ over the entire mass range. Press–Schechter does agree at the high mass end while Sheth–Tormen results in a better agreement at lower masses. This may be an indication of the more substantial role of external tidal forces on the evolution of the low-mass haloes. Such external influences are entirely ignored by the Press–Schechter formalism, while they are successfully modelled by the Sheth–Tormen fits (Sheth & Tormen 1999).

7 SHAPES OF BOUND STRUCTURES

While the formation and evolution of structure on large scales comes to a halt once the Universe starts to accelerate, the internal evolution of overdense patches continues. One of the most telling manifestations of the internal evolution of these collapsing objects is their changing shape. The substructures that are within the bound radius will merge with each other into an increasingly smooth and concentrated clump that will gradually assume a more and more spherical configuration.

Using a variety of definitions for superclusters, their shape has been studied both using real data (e.g. Plionis et al. 1992; Sathyaprakash et al. 1998; Basilakos et al. 2001; Sheth et al. 2003; Einasto et al. 2007c) and in N-body simulations (e.g. Sathyaprakash, Sahni & Shandarin 1998; Shandarin, Sheth & Sahni 2004; Basilakos et al. 2006; Wray et al. 2006; Einasto

et al. 2007c). Most studies agree that the dominant shape of superclusters at the present time is prolate, which is most evident in the presence of elongated filaments. These predominantly anisotropic shapes are a clear indication of the quasi-linear dynamical stage at which we find the present-day superclusters.

7.1 Definitions

In order to determine the shape, we calculate the inertia tensor using all particles inside the spheres defined by equation (13) with respect to their centre of mass:

$$I_{ij} = \sum x_i x_j m. \tag{27}$$

Since the matrix is symmetric, it is possible to find a coordinate system such that it is diagonal, yielding the eigenvalues a_1, a_2 and a_3. These give a quantitative measure of the degree of symmetry of the distribution. With the major axis s_1, medium axis s_2 and minor axis s_3, i.e. $s_3 < s_2 < s_1$, the two axis ratios s_2/s_1 and s_3/s_1 are given by
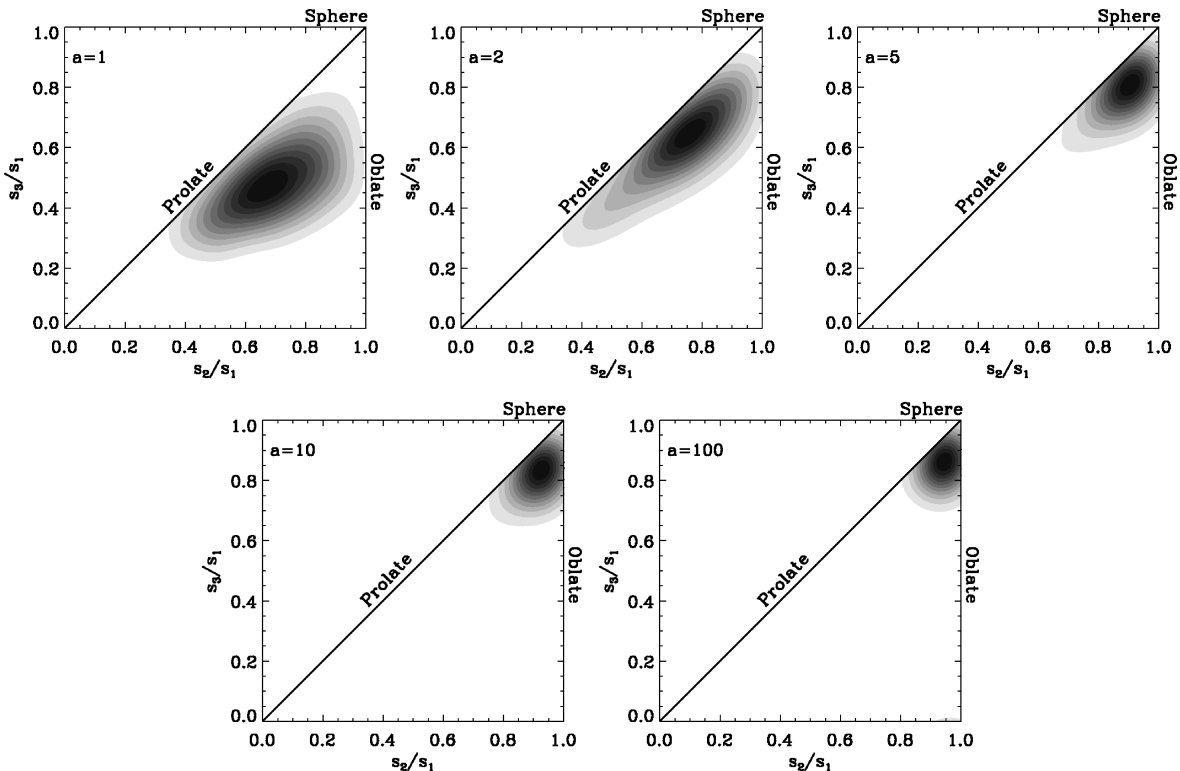
$$\frac{s_2}{s_1} = \sqrt{\frac{a_2}{a_1}}, \qquad \frac{s_3}{s_1} = \sqrt{\frac{a_3}{a_1}}, \tag{28}$$

where $a_1 > a_2 > a_3$.

The object is almost spherical if both ratios s_2/s_1 and s_3/s_1 are close to one. Oblate objects have axis ratios $s_3 \ll s_2 \sim s_1$, prolate objects $s_3 \sim s_2 \ll s_1$.

7.2 Shape evolution

Fig. 10 reveals the overall evolving shape distribution from the present epoch until $a = 100$. The shape distribution is shown in

Figure 10. Distribution of axis ratios for bound objects at five different expansion factors. Top row: $a = 1$, 2 and 5; bottom row: $a = 10$ and $a = 100$. Each diagram shows the probability density distribution in the plane of s_2/s_1 versus s_3/s_1 values, with principal axes $s_3 < s_2 < s_1$. Plotted is the axis ratio probability distribution in iso-probability grey-scale values, with percentile steps of 10 per cent. Dark colours correspond to high probability, decreasing to lower probabilities as colours fade to light (in steps of 5 per cent).

Table 2. Average values of the axis ratios s_2/s_1 and s_3/s_1, with their standard deviation, at five expansion factors: $a = 1$, $a = 2$, $a = 5$, $a = 10$ and $a = 100$.

	$\langle s_2/s_1 \rangle$	$\langle s_3/s_1 \rangle$	σ_{s_2/s_1}	σ_{s_3/s_1}
$a = 1$	0.69	0.48	0.13	0.11
$a = 2$	0.73	0.61	0.14	0.13
$a = 5$	0.87	0.77	0.10	0.10
$a = 10$	0.90	0.81	0.08	0.08
$a = 100$	0.94	0.85	0.03	0.05

terms of a plot of the axis ratios s_2/s_1 versus s_3/s_1 of the objects. The corresponding shape distribution function is shown by means of grey-scale iso-probability contour maps. Because by definition $s_3 < s_2 < s_1$, only the right-hand triangle of the diagram is populated. Spherical groups are located at (1, 1), oblate groups tend towards the line $s_2/s_1 = 1$, while prolate groups are found near the diagonal $s_2/s_1 = s_3/s_1$.

At the first two time-steps, $a = 1$ and $a = 2$, we find a clear dominance of non-spherical objects. Most objects are distinctly anisotropic, which agrees with the observations of individual objects in Section 4. At $a = 1$ the objects occupy a wide range of mostly triaxial shapes, with a mean value $(\langle s_2/s_1 \rangle, \langle s_3/s_1 \rangle) = (0.69, 0.48)$ and a standard deviation of $(\sigma_{s_2/s_1}, \sigma_{s_3/s_1}) = (0.13, 0.11)$ (see Table 2). There are hardly any thin pancake-shaped structures, as low values of $s_3/s_1 < 0.25$ seem to be absent. To some extent this may be a reflection of our bound group identification procedure, given its bias towards spherical configurations (see Section 3.1.6). Starting at $a = 2$ we observe a stretching of the shape distribution (Fig. 10), along the direction of the prolate configurations, $s_3/s_1 = s_2/s_1$, and towards less anisotropic and more spherical morphologies. A sizeable fraction of the objects shows a tendency towards a prolate shape.

The fact that there are almost no spherical, or even nearly spherical objects, at the earlier epochs is hardly surprising given the relative youth of these supercluster objects. It is a reflection of the fact that the primordial density field does not contain spherical peaks (Bardeen et al. 1986) and that the first stages of gravitational contraction and collapse proceed via strongly flattened and elongated geometries (Zeldovich 1970; Icke 1973).

After $a = 2$, there is a rapid evolution of the vast majority of objects towards a nearly spherical shape. At $a = 5$ nearly all clumps are found in the corner with the axis ratio $s_2/s_1 = s_3/s_1 = 1$. Also after $a = 5$ the width of the shape distribution continues to shrink. Not only do the bound clumps and superclusters on average attain a more spherical shape as the expansion of the Universe accelerates, it is the entire population of objects that appears to follow this trend. This systematic change of shape can be most clearly appreciated from the inspection of Table 2.

In all, the contrast between the shape distribution at $a = 1$ and the one at $a = 100$ reveals a manifest and even radical internal evolution of the supercluster complexes, at the same time when evolution on larger scales has been virtually frozen.

7.3 Mass dependence

One potentially relevant issue concerns the possible dependence of shape on the mass of bound structures. In order to investigate this, we divide our sample in three mass ranges, all approximately including the same number of bound structures. Class I consists of the most massive third of objects, which at $a = 1$ have a mass $M >$

$4.8 \times 10^{14} \, h^{-1} \, \mathrm{M}_\odot$. The medium mass class II includes objects with masses at $a = 1$ of $2.8 \times 10^{14} \, h^{-1} \, \mathrm{M}_\odot < M \leq 4.8 \times 10^{14} \, h^{-1} \, \mathrm{M}_\odot$ and the low-mass class III consists of objects with masses at $a = 1$ of $2 \times 10^{14} \, h^{-1} \, \mathrm{M}_\odot < M \leq 2.8 \times 10^{14} \, h^{-1} \, \mathrm{M}_\odot$.

We found that over the entire interval of $a = 1$ to $a = 100$, there is hardly any distinction between the shape distribution in the different mass ranges (see Fig. 11). The three mass ranges have similar mean axis ratios at all five expansion factors (see Table 3). This must be related to the fact that even though of different masses, the objects have been selected on the basis of similar (over)density values. The latter is an indication for the evolutionary state of the objects. In turn, as we have seen, this is reflected in their shape.

We conclude that irrespective of their masses, all objects evolve into single, virialized and spherical objects as they grow in complete isolation after the Universe assumed an accelerated expansion and after all surrounding clumps and substructure within their binding radius has been accreted.

7.3.1 Cluster versus supercluster shapes

Keeping in mind that the objects in our sample are bound but perhaps not virialized, it is instructive to contrast them to virialized galaxy clusters. Although their masses may be comparable, the bound group radii are much larger as they have substantially lower densities than clusters. Within this larger region, there is a considerably more pronounced substructure.

At $a = 1$, the clusters in our simulation are triaxial, with average axis ratios $(\langle s_2/s_1 \rangle, \langle s_3/s_1 \rangle) = (0.83, 0.71)$ and standard deviation $(\sigma_{s_2/s_1}, \sigma_{s_3/s_1}) = (0.09, 0.09)$. These values are somewhat more pronounced than those quoted in other studies (e.g. Dubinski & Carlberg 1991; Katz 1991; van Haarlem & van de Weygaert 1993; Jing & Suto 2002; Kasun & Evrard 2005; Paz et al. 2006; Allgood et al. 2006). All agree that they tend to be more prolate as the halo mass increases. Dubinski & Carlberg (1991) found that haloes are 'strongly triaxial and very flat', with mean axis ratios of $\langle s_2/s_1 \rangle = 0.71$ and $\langle s_3/s_1 \rangle = 0.50$. For simulations of isolated haloes with different power spectra indices, Katz (1991) found s_2/s_1 values ranging from ≈ 0.84 to 0.93 and s_3/s_1 from ≈ 0.43 to 0.71, while for massive clusters Kasun & Evrard (2005) found peak values of $(s_2/s_1, s_3/s_1) = (0.76, 0.64)$.

Even though the radii of the bound structures in our sample are considerably larger than the virial radii of clusters, they do have similar triaxial shapes. None the less, we do notice a distinct tendency of the superclusters to be more anisotropic than that of the virialized clusters. This must be a reflection of their different dynamical states.

8 INTERNAL MASS DISTRIBUTION AND DENSITY PROFILES

We have seen that superclusters are gradually decoupling from the global cosmic expansion, and towards the far future evolve in isolation as genuine *cosmic islands*. As these contract and collapse, and finally even virialize, they will develop into a much more compact object. To understand their internal evolution, it is important to look into the development of their internal mass distribution, and hence their density profile.

8.1 Supercluster case studies

Before trying to draw some general conclusions, we look in more detail at the evolving mass distribution inside and around two
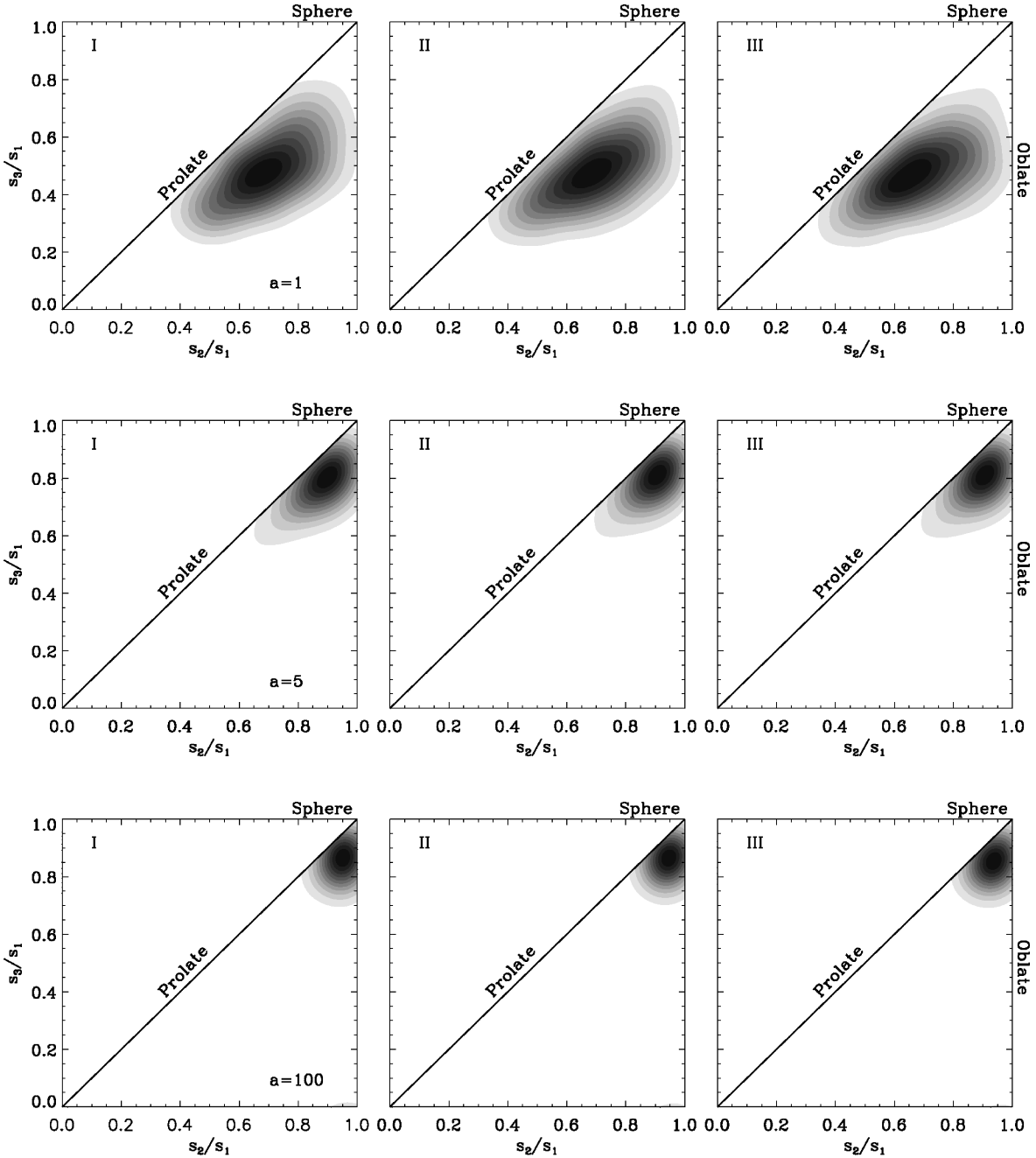
Figure 11. Distribution of axis ratios for three mass ranges. I: high-mass bound objects with $M > 4.8 \times 10^{14} \, h^{-1} \, \mathrm{M_\odot}$. II: medium mass range bound objects, $2.8 \times 10^{14} \, h^{-1} \, \mathrm{M_\odot} < M \leq 4.8 \times 10^{14} \, h^{-1} \, \mathrm{M_\odot}$. III: low-mass bound objects, $2 \times 10^{14} \, h^{-1} \, \mathrm{M_\odot} < M \leq 2.8 \times 10^{14} \, h^{-1} \, \mathrm{M_\odot}$. Each diagram shows the probability density distribution in the plane of s_2/s_1 versus s_3/s_1 values, with principal object axes $s_3 < s_2 < s_1$. Dark colours correspond to high probabilities, decreasing to lower probabilities as colours fade to light, with level steps corresponding to percentile differences of 10 per cent. Top row: axis ratio distribution at the current epoch, $a = 1$. Middle row: axis ratio distribution at $a = 5$. Bottom row: axis ratio distribution at $a = 100$.

representative individual superclusters in our sample. These are objects 8 and 98. The first one is a massive supercluster with a mass of $\sim 5.4 \times 10^{15} \, h^{-1} \, \mathrm{M_\odot}$, while the second one has a mass of $\sim 3.6 \times 10^{15} \, h^{-1} \, \mathrm{M_\odot}$. Supercluster 8 is one of the most massive objects identified at $a = 1$ and also ends up as such at $a = 100$.

The evolution of the mass distribution in and around superclusters 8 and 98 from a web-like irregular and structured pattern at $a = 1$ into smooth and highly concentrated and nearly spherical mass clumps at $a = 100$ can be observed from the changing particle distributions in the left-hand and central frames of Fig. 12. For

guidance, on all four panels we superimposed circles centred at the supercluster's core. These are the 'half-mass sphere' (solid circle), enclosing half of the total mass of the supercluster, and the 'virial sphere', enclosing the central virialized core of the supercluster (dash–dotted circle).

For the structure of the virial core, we turn to the log–log diagrams of the radial density profiles $\rho(r)$ in Fig. 13. All profiles have the same basic shape, a high density central core embedded within an isothermal power-law region with slope ~ -2. While there may still be some deviations from this slope at $a = 1$,

Table 3. Number of objects and average values of the axis ratios s_2/s_1 and s_3/s_1, with their standard deviation, at $a = 1$, $a = 5$ and $a = 100$ for three mass intervals (with mass range set at $a = 1$).

|			$\langle s_2/s_1 \rangle$	$\langle s_3/s_1 \rangle$	σ_{s_2/s_1}	σ_{s_3/s_1}
I.	$M > 4.8 \times 10^{14}\, h^{-1}\, M_\odot$	$a = 1$	0.70	0.49	0.13	0.11
		$a = 2$	0.72	0.60	0.13	0.12
		$a = 5$	0.86	0.76	0.10	0.10
		$a = 10$	0.90	0.81	0.07	0.08
		$a = 100$	0.94	0.85	0.03	0.05
II.	$2.8 \times 10^{14}\, h^{-1}\, M_\odot < M \leq 4.8 \times 10^{14}\, h^{-1}\, M_\odot$	$a = 1$	0.70	0.48	0.13	0.11
		$a = 2$	0.74	0.63	0.14	0.13
		$a = 5$	0.87	0.77	0.09	0.10
		$a = 10$	0.91	0.81	0.07	0.08
		$a = 100$	0.94	0.85	0.03	0.05
III.	$2 \times 10^{14}\, h^{-1}\, M_\odot < M \leq 2.8 \times 10^{14}\, h^{-1}\, M_\odot$	$a = 1$	0.68	0.47	0.14	0.11
		$a = 2$	0.73	0.62	0.15	0.14
		$a = 5$	0.86	0.76	0.11	0.11
		$a = 10$	0.90	0.80	0.08	0.08
		$a = 100$	0.93	0.85	0.04	0.05

comparison with the inserted short line of slope -2 shows that at $a = 100$ the object cores are almost perfectly isothermal. The profiles confirm the impression from Fig. 12 of the growth of the virial core, given the smooth near power-law profiles at $a = 100$ as opposed to the more irregular behaviour at the outer edges in the $a = 1$ profiles.

In addition, we note a radical change of the cosmic surroundings of both superclusters. At $a = 1$, both superclusters are still solidly

integrated and embedded within the megaparsec cosmic web. Their central cores, indicated by the 'virial spheres', are connected to the surroundings via filamentary tentacles along which we find a large variety of mass clumps. Note that these outer structures at $a = 1$ are actually bound to the supercluster core and will fall in and merge with the central cluster as time proceeds. At $a = 100$ the resulting supercluster concentrations have turned into isolated islands.
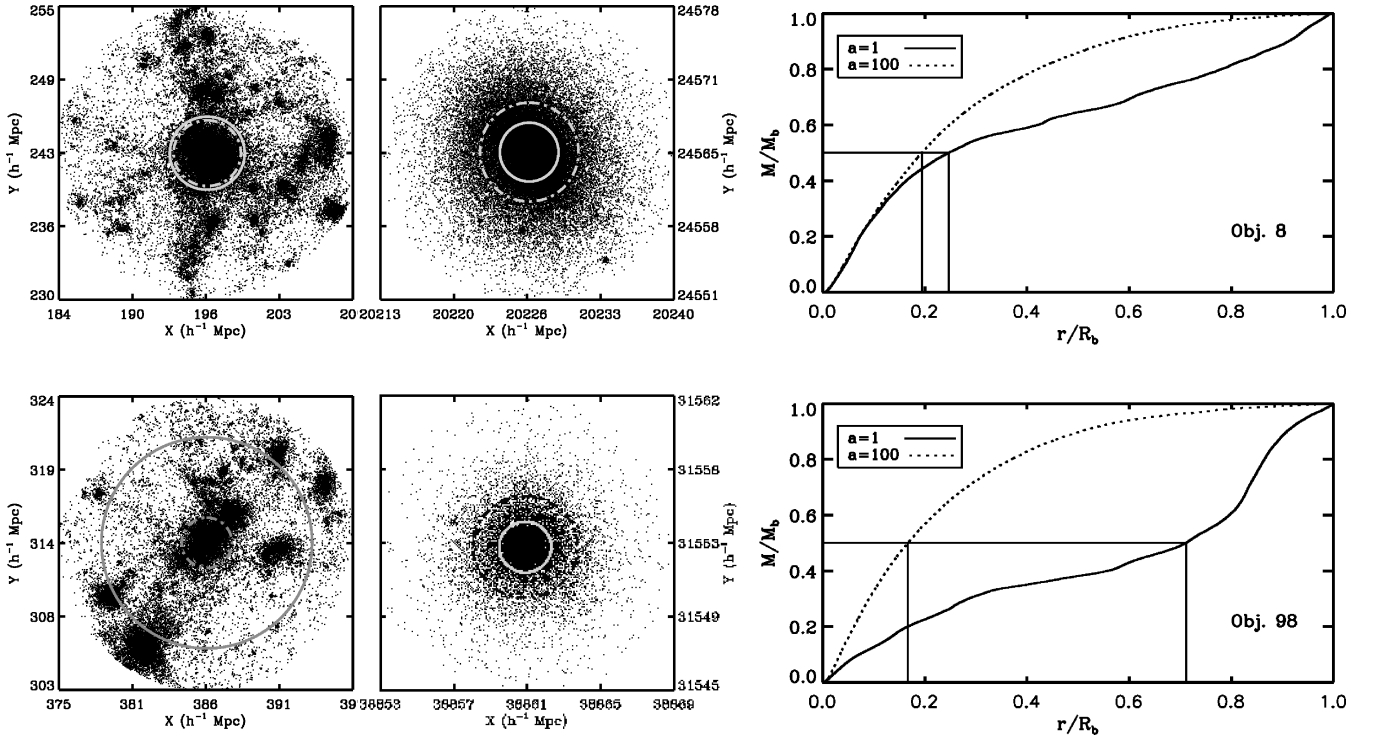
Figure 12. Top: supercluster 8 ($M \sim 5.4 \times 10^{15}\, h^{-1}\, M_\odot$). Bottom: supercluster 98 ($M \sim 3.6 \times 10^{15}\, h^{-1}\, M_\odot$). Dark matter/particle distribution at $a = 1$ (left) and $a = 100$ (centre) of object 8, in physical coordinates. For comparison, the half-mass radius (solid circle) and the virial radius (dash–dotted circle) are superimposed on the matter distribution. Right-hand panel: cumulative mass distribution of the object as a function of its (normalized) radius r/r_b, at $a = 1$ (solid line) and at $a = 100$ (dotted line). The cumulative mass M/M_b is normalized with respect to the corresponding final (bound) mass M_b. The solid vertical lines indicate the value of the half-mass radius (for which $M/M_b = 0.5$, the horizontal solid line), at both epochs $a = 1$ and $a = 100$.
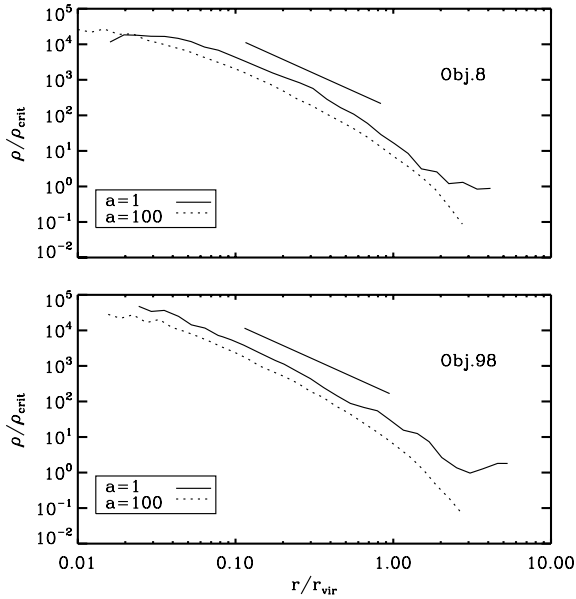
Figure 13. Radial density profiles of object 8 (top panel) and object 98 (bottom panel). In a log–log diagram, each of the panels shows the radial density profile $\rho(r)$, in units of the critical density $\rho_{\rm crit}$, as a function of the normalized radius $r/r_{\rm vir}$ (normalized with respect to the supercluster virial radius). Solid line: profile at $a = 1$. Dotted line: profile at $a = 100$. For comparison in both panels, we include a short line with an isothermal slope -2.

It is telling that at $a = 100$ both superclusters have attained an almost equivalent internal mass distribution, even though at $a = 1$ their morphology was quite different. At the present epoch, supercluster 8 is already a centrally concentrated object. Given that the half-mass and virial spheres nearly overlap, we see that at $a = 1$ its virialized core contains nearly half of its total mass. This impression is underlined by the cumulative mass distribution in the right-hand panel of Fig. 12. Comparison between the cumulative mass distribution at $a = 1$ (solid line) and $a = 100$ (dashed line) shows that there is only a small increase in mass in the inner region of the supercluster, immediately around the virialized core. Also, the fact that the half-mass radius moves only slightly inward implies a moderate change in the inner mass distribution. It is the outer half of the supercluster's mass which rearranges itself more strongly: as it falls in towards the supercluster's interior, the mass distribution becomes more concentrated and more regular.

The changing mass distribution is more pronounced for supercluster 98. At the current epoch its mass distribution is more extended: its half-mass radius is located at an outward position. The central core is not nearly as prominent as that in supercluster 8. The supercluster's mass increases rather slowly until the half-mass radius. Beyond this radius, there is an abrupt rise until the outer supercluster radius. This is related to the presence of another major mass clump near the outer boundary. When we would have observed this supercluster in the observational reality, we would find it to be dominated by two very rich clusters.

Also, we note that the superclusters do hardly gain mass from beyond their (binding) radius $R_{\rm b}$. This is reflected in the flattening of the cumulative mass curves at $a = 100$.

8.2 Supercluster mass concentration

From the discussion in the previous section, we have learned that the superclusters are turning into bodies with a highly concentrated

mass distribution at $a = 100$. It is only towards these later cosmic epochs that the superclusters have turned into highly non-linear and concentrated regions. It would not be appropriate to seek to fit a theoretical density profile to their radial mass distribution in order to determine their concentration. Instead of seeking to fit an Einasto profile (Einasto 1965), or the profusely popular universal NFW profile (Navarro, Frenk & White 1997), we therefore prefer to define a concentration parameter that is independent of assumptions about the dynamical state of the mass concentration,

$$c = \frac{r_{\rm hm}}{r_{\rm b}}, \qquad (29)$$

where $r_{\rm hm}$ is the radius that encloses half of the mass. Note that with this definition a mass distribution with a 'delta peak' at the centre would have $c = 0$, while a perfectly uniform distribution would have $c \approx 0.8$. An isothermal distribution would correspond to $c = 0.5$.

Fig. 14 shows the distribution of c as a function of mass, for the object population at $a = 1$ until $a = 100$. At the present epoch, there is still a considerable spread of the concentration parameter ($\bar{c} = 0.35$, $\sigma_c = 0.14$). There are even a few objects that get close to the $c = 0.8$ value corresponding to uniform mass profiles. Although there is a slight tendency towards higher concentrations, in general the concentration parameter at $a = 1$ reflects the irregular and prominent outer mass distribution. Low-mass bound objects appear to be more strongly concentrated than the $M > 10^{15}\,h^{-1}\,{\rm M_\odot}$ superclusters.

The additional panels reveal the expected development. After $a = 1$, there is a relatively rapid evolution towards much more concentrated configurations. While at $a = 2$, there are still a sizeable number of bound objects and superclusters with a rather diffuse or uniform internal mass distribution, at $a = 5$ nearly all objects have attained a high level of concentration of $c < 0.4$, with most having a concentration index $c \sim 0.2$. This development continues towards a radical conclusion at around $a = 10$. Over the whole mass range objects are highly concentrated from $a = 10$ onward. Also note that the trend of low-mass objects to be more concentrated than high-mass superclusters persists, even though it gradually weakens towards later epochs. At the final time of $a = 100$, nearly all objects have $c < 0.2$, with an average concentration index $\bar{c} = 0.16$ and $\sigma_c = 0.02$.

It is clear that this evolution ties in strongly with the tendency to assume a near perfect spherical shape and, as we will see in the next section, with a rapidly decreasing level of substructure and multiplicity of the superclusters.

9 SUPERCLUSTER SUBSTRUCTURE AND MULTIPLICITY FUNCTION

The third aspect of the internal evolution of superclusters is that of their substructure. Because superclusters are usually identified via their cluster content, we focus on their *multiplicity* $N_{\rm SC}$, i.e. the number of clusters they contain. Clusters are taken to be virialized subclumps with a mass higher than $3 \times 10^{13}\,h^{-1}\,{\rm M_\odot}$, the low-mass threshold for the virialized groups at $a = 1$. We should take into account that the definition of the multiplicity $N_{\rm SC}$ depends on the cluster mass threshold in our sample.

Fig. 15 gives an impression of the substructure of one of the superclusters in our sample, at $a = 1$. The cluster population within the supercluster is indicated by circles. The supercluster area is still a rather polymorphic assembly of matter, connected by means
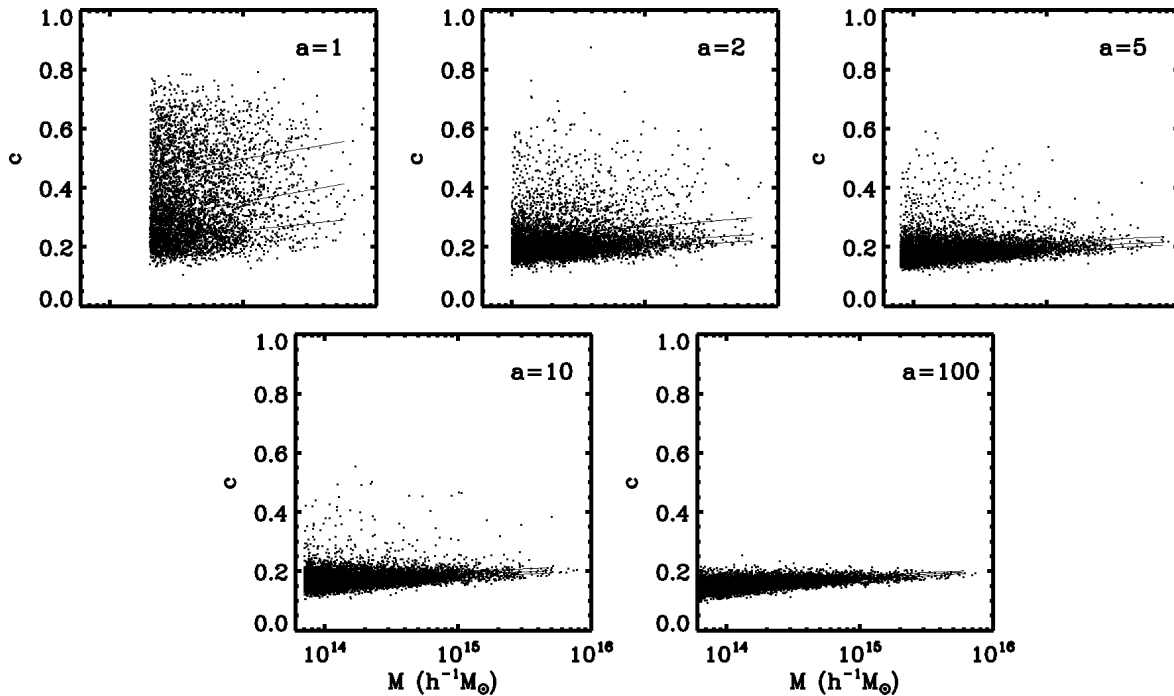
Figure 14. Concentration parameter c of each bound object in the bound object sample as a function of its mass M. The concentration parameter is the ratio of the half-mass radius of the object to its total binding radius $r_{b,c} \equiv r_{hm}/r_b$. Superimposed on each of the plots is the line indicating the median in mass bins, along with the corresponding 25 and 75 percentile lines. Left-hand panel: $a = 1$. Right-hand panel: $a = 100$. At $a = 100$ nearly all objects have a highly concentrated mass distribution, i.e. $c < 0.2$. Note that the bound object sample is different at each expansion factor (see Section 3.1.9).

of filamentary extensions. The most prominent concentrations, the clusters, roughly follow these web-like structures.

Interestingly, we find that the mean mass of all the clusters in our simulation volume is $M_{cl} = 9.4 \times 10^{13} \, h^{-1} \, M_{\odot}$ while those residing within the realm of superclusters have an average mass $M_{cl} = 3.6 \times 10^{14} \, h^{-1} \, M_{\odot}$. The fact that superclusters contain more massive clusters is partly a result of the stronger clustering of higher mass clusters (Kaiser 1984; Bahcall 1988). An additional factor is the active dynamical environment inside superclusters. Because of the high concentration of subclumps, these are continuously merging and falling into ever more massive clumps. Clusters will

Figure 15. Supercluster multiplicity. The (dark) mater distribution within the binding radius of a supercluster, at $a = 1$. The clusters within the supercluster realm are indicated by circles. The size of the circle reflects the (virial) size of each cluster halo.

be centres of action and thus grow rapidly in mass. Meanwhile, lower mass and lower density clumps are more liable to lose mass or even to get gradually dismantled by the prevailing strong tidal forces in and near the superclusters.
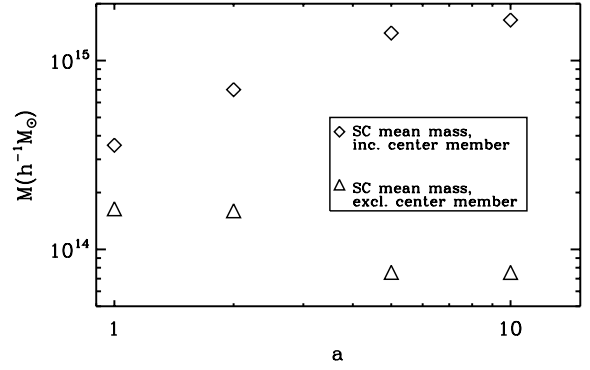
9.1 Multiplicity evolution

One of the principal findings of our study is that, without exception, at $a = 100$ all superclusters in our sample have attained a multiplicity one. By that time, they all have evolved into compact and smooth density concentrations, akin to the one seen in Fig. 3. The hierarchical development of the supercluster involves the gradual merging of its constituent subclumps into one condensed object. As a result, we see that superclusters which at the present epoch contain several to dozens of clusters ultimately end up as an object of unit multiplicity. Fig. 16 reveals the systematic evolution towards this configuration.

Turning to the present epoch, we assess the multiplicity function for the 17 most massive superclusters, those whose mass is in excess of $M = 5 \times 10^{15} \, h^{-1} \, M_{\odot}$. When evaluating the (cumulative) multiplicity distribution, the number density of superclusters with more than N_{SC} clusters (Fig. 16, top-left row), we see that half of the superclusters have 10 or more members. Another important trend, not entirely unexpected, is that larger and more massive superclusters contain a higher number of cluster members. One can immediately infer this when looking at the multiplicity N_{SC} against supercluster mass M_{SC}, plotted in the right-hand row of Fig. 16. This trend is particularly strong for superclusters with $N_{SC} < 10$. For a reason which we do not entirely understand, the multiplicity seems to level off for more massive and larger supercluster complexes.

At first gradually, at $a = 2$, and later more radically we see a strong change in the multiplicity N_{SC} of superclusters as more and
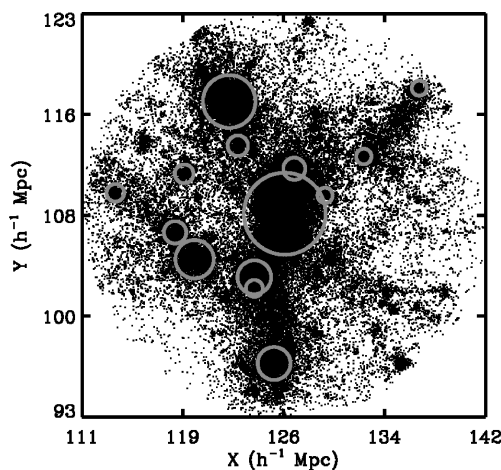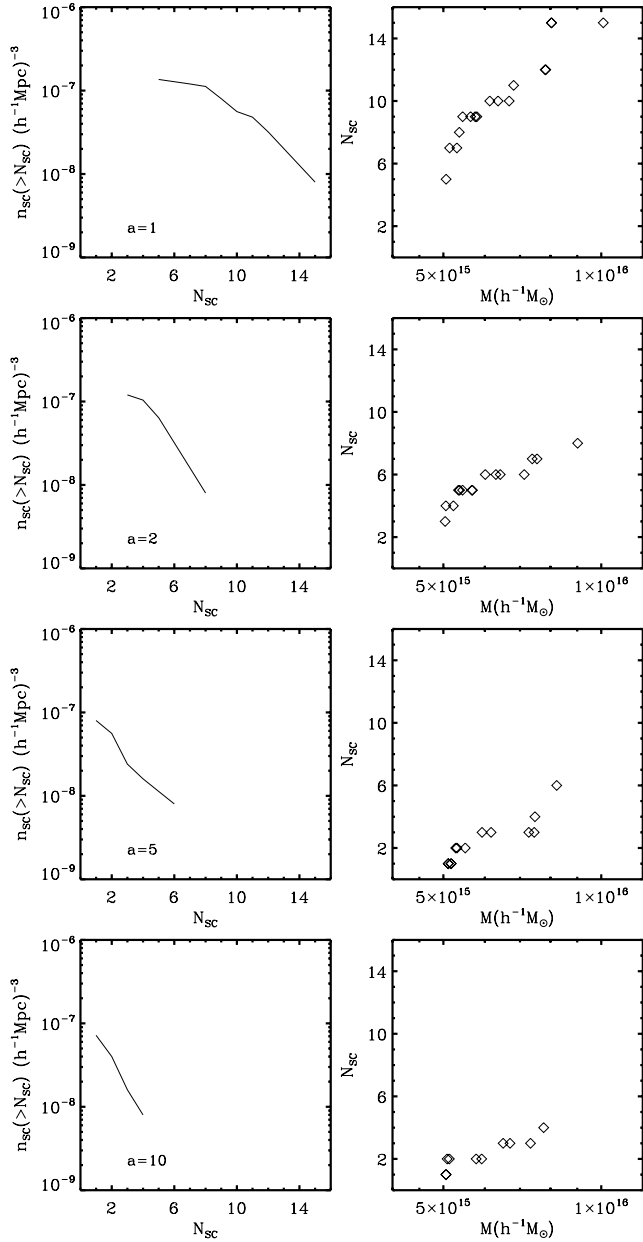
Figure 16. Supercluster multiplicity. Left-hand panel: the cumulative multiplicity distribution $n_{SC}(N_{SC})$ of superclusters containing N_{SC} or more clusters at four different expansion factors: $a = 1$, $a = 2$, $a = 5$ and $a = 10$. At each time-step the distribution concerns the most massive superclusters in the simulation, with $M > 10^{15}\,h^{-1}\,\mathrm{M}_\odot$. Right-hand panel: supercluster multiplicity N_{SC} as a function of the mass M of the supercluster.

Figure 17. Mean mass of the cluster members of superclusters in our sample, including (diamonds) and excluding (triangles) the central mass concentration.

superclusters that still have more than one cluster member appear to have less and less clusters within their realm.

An additional interesting issue is that of the masses of the clusters that populate superclusters. In Fig. 17 we can see that the mean mass of clusters in superclusters is continuously growing, from $M_{cl} = 7 \times 10^{14}\,h^{-1}\,\mathrm{M}_\odot$ at $a = 2$ to $M_{cl} = 1.6 \times 10^{15}\,h^{-1}\,\mathrm{M}_\odot$ at $a = 10$. However, this reflects the continuous growth of the central mass concentration, accompanied by the decreasing supercluster multiplicity: the mean mass becomes more and more dominated by that of the central supercluster core. Meanwhile, the mass of the remaining clusters outside the core decreases. In other words, the first clusters to merge with the supercluster core tend to be its most massive companions. The ones that accrete at a later epoch have a considerably lower mass. This is in accordance with our observation in Section 4 (see Fig. 3).

9.2 Multiplicity criterion

Because we have used a physical criterion for the identification of clusters and superclusters, we assume the inferred multiplicities to be close to the one found in the observed reality. To some extent, supercluster multiplicity estimates will depend on the supercluster identification procedure. There is certainly a dependence on percolation radius when identified on the basis of a percolation criterion (Zeldovich, Einasto & Shandarin 1982; Shandarin & Zeldovich 1989).

This may be one of the reasons why our measured supercluster multiplicities differ from those obtained in other studies (in addition to the dependence on cluster mass threshold). For example, Wray et al. (2006) found superclusters with more than 30 members. This certainly relates to the choice of linking length for defining the supercluster: dependent on the linking length they found maximum supercluster sizes ranging from ∼30 to ∼150 h^{-1} Mpc. The latter are much larger than the superclusters we find according to our definition based on binding density.

10 SHAPLEY-LIKE SUPERCLUSTERS

The Shapley concentration, first noted by Shapley (1930), is one of the most outstanding supercluster complexes out to $z = 0.12$ (see Raychaudhury 1989; Ettori, Fabian & White 1997; Quintana et al. 2000; Proust et al. 2006). It amasses at least 30 rich Abell galaxy clusters in a core region of ∼25 h^{-1} Mpc and is located at a distance of ∼140 h^{-1} Mpc. Its total mass is estimated to be

more clusters within their realm merge and mix with the central matter concentration. The left-hand column of panels shows the systematic decline of high multiplicity objects. At $a = 2$ we can no longer find superclusters with more than 10 cluster members. At that epoch two of the 17 superclusters have collapsed into a single object of multiplicity 1. Towards the later epochs the multiplicity of superclusters quickly declines further, and at $a = 10$ there are no superclusters around with more than five clusters.

When looking at the corresponding frames for the multiplicity as a function of supercluster mass, we see that the number of superclusters of unit multiplicity is continuously increasing. Meanwhile, the

$\sim 5 \times 10^{16}\, h^{-1}\, \mathrm{M_{\odot}}$ within a radius of $\sim 30\, h^{-1}\, \mathrm{Mpc}$ (see e.g. Proust et al. 2006; Muñoz & Loeb 2008). Almost as massive is another similar assembly of massive clusters in the local Universe, the Horologium–Reticulum supercluster (see e.g. Fleenor et al. 2005). Both may have a major influence on the motion of the Local Group with respect to the background Universe (see e.g. Plionis & Valdarnini 1991; Kocevski & Ebeling 2006).

We investigated in how far we can find back the equivalents of the Shapley and Horologium superclusters in our simulation. On the basis of the mass functions determined in Section 6.2, we estimate that the most massive supercluster present in a volume akin to the local Universe ($z < 0.1$) may have a mass of $\sim 8 \times 10^{15}\, h^{-1}\, \mathrm{M_{\odot}}$. This mass is slightly larger than the one in the bound region of the Shapley concentration as determined by Dünner et al. (in preparation). Extrapolating this conclusion, we find that one may typically find two Shapley-like superclusters out to $z \approx 0.1$, a volume of the size of the Local Universe.

When turning towards the multiplicity of the detected simulation superclusters, we find from Fig. 16 that the largest supercluster in the Local Universe would have 15 members. A Shapley-like supercluster would have a radius of $\sim 14\, h^{-1}\, \mathrm{Mpc}$ and host between 10 and 15 members, close to the number found in the bound region of the Shapley supercluster (Dünner et al., in preparation), which contains $\sim 1/3$ of the clusters traditionally assigned to this structure (e.g. Proust et al. 2006). In the observational reality of our Local Universe ($z < 0.1$), we find five superclusters with 10 or more members, the largest one containing 12 members (see e.g. Einasto et al. 1994).

This brings us to the issue of the extent to which the supercluster population in our ΛCDM simulation at $a = 1$ resembles the one seen in our nearby Universe. To this end, we are in the process of translating our theoretical supercluster criterion into one that would be able to identify structures along the same lines in large magnitude-limited galaxy redshift surveys. By applying this to the 6dF galaxy sample (Jones et al. 2009) and the SDSS DR7 galaxy sample (Abazajian et al. 2009), we plan a detailed comparison of morphology, size and spatial distribution of the identified superclusters with those seen in our simulation. First indications from similar comparison between superclusters in the 2dFGRS sample (Colless et al. 2003) and the Millennium simulation (Springel et al. 2005), based on a more conventional supercluster identification process, seems to indicate that there are no discernable discrepancies (Einasto et al. 2007b).

11 CONCLUSIONS

In this work, we have followed the evolution of bound objects from the present epoch up to a time in the far future of the Universe, at $a = 100$, in a standard ΛCDM ($\Omega_{m,0} = 0.3$, $\Omega_{\Lambda,0} = 0.7$ and $h = 0.7$) Universe. We contrasted the external global evolution of the population of bound objects with their vigorous internal evolution, starting from the contention that in a dark energy dominated Universe they have the character of *island universes*. Within such a Universe, we expect them to become increasingly isolated objects in which cosmic evolution proceeds to the ultimate equilibrium configuration of a smooth, spherical, virialized and highly concentrated mass clumps. We identify the most massive of these objects with superclusters.

For the external evolution, we investigate the spatial distribution and clustering of bound objects and superclusters, along with the weak change of their mass functions. To assess the internal structure, we have looked into their rapidly changing shape, their evolving

density profile and mass concentration and the level of substructure of the superclusters in terms of their multiplicity, i.e. the number of clusters within their realm.

We defined the bound structures by the density criterion derived in Paper I (see equation 13), and identified them from a $500\, h^{-1}\, \mathrm{Mpc}$ cosmological box with 512^3 dark matter particles in a ΛCDM ($\Omega_{m,0} = 0.3$, $\Omega_{\Lambda,0} = 0.7$ and $h = 0.7$) Universe. We ran the simulation up to $a = 100$, which is a time where structures have stopped forming. We used the HOP halo identifier in order to identify independently virialized structures, at each of the five time-steps we have analysed in detail: $a = 1, 2, 5, 10$ and 100.

The main results of the present study can be summarized as follows.

(i) While the large-scale evolution of bound objects and superclusters comes to a halt as a result of the cosmic acceleration, their internal evolution continues vigorously until they have evolved into single, isolated, almost perfectly spherical, highly concentrated, virialized mass clumps. This development is very strong between $a = 1$ and 10, and continues up to $a = 100$.

(ii) The marginally bound objects that we study resemble the superclusters in the observed Universe. While clusters of galaxies are the most massive, fully collapsed and virialized objects in the Universe, superclusters are the largest bound – but not yet collapsed – structures in the Universe.

(iii) The superclusters are true *island universes*: as a result of the accelerating expansion of the Universe, no other, more massive and larger, structures will be able to form.

(iv) While the superclusters collapse between $a = 1$ and $a = 100$, their surroundings change radically. While at the present epoch they are solidly embedded within the cosmic web, by $a = 100$ they have turned into isolated cosmic islands.

(v) The large-scale distribution of bound objects and superclusters (in comoving space) does not show any significant evolution in between $a = 1$ and $a = 100$. The cluster and supercluster correlation functions do not change over this time interval, and retain their near power-law behaviour. Superclusters remain significantly stronger clustered than the average bound object, with a supercluster correlation length of $23 \pm 5\, h^{-1}\, \mathrm{Mpc}$ compared to $r_0 \approx 11.5\, h^{-1}\, \mathrm{Mpc}$ for the full bound object distribution in our simulation sample.

(vi) The mass functions of bound objects and superclusters hardly change from $a = 1$ to $a = 100$, as we expect on theoretical grounds. The mass functions in the simulations are generally in good agreement with the theoretical predictions of the Press–Schechter, Sheth–Tormen and Jenkins mass functions. At $a = 1$, the Sheth–Tormen prescription provides a better fit. At $a = 100$, the pure Press–Schechter function seems to be marginally better. This may tie in with the more anisotropic shape of superclusters at $a = 1$ in comparison to their peers at $a = 100$.

(vii) The change in the internal mass distribution and that in the surroundings is directly reflected by the radial density profile. Without exception towards $a = 100$ all objects attain a highly concentrated internal matter distribution, with a concentration index $c = 0.2$. In general, the vast majority of objects has evolved into a highly concentrated mass clump after $a = 10$.

(viii) The mass profile in the outer realms of the supercluster changes radically from $a = 1$ to $a = 100$. At $a = 1$ it is rather irregular, while there are large differences between the individual objects. This is a reflection of the surrounding inhomogeneous mass distribution of the cosmic web. In between $a = 5$ and $a = 10$, nearly all superclusters have developed a smooth, regular and steadily declining mass profile.

(ix) The inner density profile steepens substantially when the inner region of the supercluster is still contracting. On the other hand, when at $a = 1$ it has already developed a substantial virialized core, the inner density profile hardly changes.

(x) As a result of their collapse, the shapes of the bound objects systematically change from the original triaxial shape at $a = 1$ into an almost perfectly spherical configuration at $a = 100$. For example, at $a = 1$ their mean axis ratios are $(\langle s_2/s_1 \rangle, \langle s_3/s_1 \rangle) = (0.69, 0.48)$. At $a = 100$, they have mean axis ratios of $(\langle s_2/s_1 \rangle, \langle s_3/s_1 \rangle) = (0.94, 0.85)$.

(xi) At the current epoch the superclusters still contain a substantial amount of substructure. Particularly interesting is the amount of cluster mass virialized objects within its realm, expressed in the so-called *multiplicity function*. Restricting ourselves to superclusters with a mass larger than $5 \times 10^{15} \, h^{-1} \, M_\odot$, of which we have 17 in our simulation sample, we find a multiplicity of 5 to 15 at the current epoch. As time proceeds there is a systematic evolution towards unit multiplicity at $a = 100$, following the accretion and merging of all clusters within the supercluster's realms.

(xii) In a volume comparable to the Local Universe ($z < 0.1$), we find that the most massive supercluster would have a mass of $\sim 8 \times 10^{15} \, h^{-1} \, M_\odot$. This is slightly more massive than the mass of the Shapley supercluster given in Dünner et al. (in preparation). When turning towards the multiplicity, we find that the largest superclusters in the Local Universe would host between 10 and 15 members, close to the number found in the bound region of the Shapley supercluster (Dünner et al., in preparation) (which contains $\sim 1/3$ of the clusters traditionally assigned to this structure; e.g. Proust et al. 2006).

While in this study we have addressed a large number of issues, our study leaves many related studies for further investigation. One of the most pressing issues concerns an assessment of the nature of our supercluster objects. This involves a comparison with other supercluster definitions, in particular in how far our density-based definition fares at the earlier epochs when most objects of similar mass will have distinct anisotropic shapes.

Also, while here we follow the evolution of superclusters in the standard ΛCDM Universe, in an accompanying publication we will systematically address the influence of dark matter and dark energy on the emerging supercluster. There we found that dark matter is totally dominant in determining the supercluster's evolution. For a preliminary, detailed report on the analysis of the role of the cosmological constant in the formation and evolution of structures, we refer to Araya-Melo (2008).

ACKNOWLEDGMENTS

REFERENCES

Abazajian K. N. et al., 2009, ApJS, 182, 543
Allgood B., Flores R. A., Primack J. R., Kravtsov A. V., Wechsler R. H., Faltenbacher A., Bullock J. S., 2006, MNRAS, 367, 1781
Araya-Melo P. A., 2008, PhD thesis, Univ. Groningen, the Netherlands
Bahcall N. A., 1988, ARA&A, 26, 631
Bahcall N. A., Soneira R. M., 1983, ApJ, 270, 20
Bahcall N. A., Dong F., Hao L., Bode P., Annis J., Gunn J. E., Schneider D. P., 2003, ApJ, 599, 814
Bardeen J. M., Bond J. R., Kaiser N., Szalay A. S., 1986, ApJ, 304, 15
Basilakos S., Plionis M., Rowan-Robinson M., 2001, MNRAS, 323, 47
Basilakos S., Plionis M., Yepes G., Gottlöber S., Turchaninov V., 2006, MNRAS, 365, 539
Bond J. R., Myers S. T., 1996, ApJS, 103, 1
Bond J. R., Cole S., Efstathiou G., Kaiser N., 1991, ApJ, 379, 440
Bond J. R., Kofman L., Pogosyan D., 1996, Nat, 380, 603
Bryan G. L., Norman M. L., 1998, ApJ, 495, 80
Busha M. T., Adams F. C., Wechsler R. H., Evrard A. E., 2003, ApJ, 596, 713
Busha M. T., Evrard A. E., Adams F. C., 2007, ApJ, 665, 1
Carroll S. M., Press W. H., Turner E. L., 1992, ARA&A, 30, 499
Chiueh T., He X.-G., 2002, Phys. Rev. D, 65, 123518
Cohn J. D., Bagla J. S., White M., 2001, MNRAS, 325, 1053
Colless M. et al., 2003, preprint (astro-ph/0306581)
Desjacques V., 2008, MNRAS, 388, 638
Dubinski J., Carlberg R. G., 1991, ApJ, 378, 496
Dünner R., Araya P. A., Meza A., Reisenegger A., 2006, MNRAS, 366, 803 (Paper I)
Dünner R., Reisenegger A., Meza A., Araya P. A., Quintana H., 2007, MNRAS, 376, 1577
Einasto J., 1965, Trudy Inst. Astrofiz. Alma-Ata, 5, 87
Einasto M., Einasto J., Tago E., Dalton G. B., Andernach H., 1994, MNRAS, 269, 301
Einasto M., Saar E., Tago E., Müller V., Andernach H., 2001, ApJ, 122, 2222
Einasto M., Einasto J., Tago E., Andernach H., Dalton G. B., Müller V., 2002, ApJ, 123, 51
Einasto J., Einasto M., Saar E. et al., 2007, A&A, 462, 397
Einasto M., Saar E., Liivamäagi L. J. et al., 2007c, A&A, 476, 697
Eisenstein D. J., Loeb A., 1995, ApJ, 439, 520
Eisenstein D. J., Hut P., 1998, ApJ, 498, 137
Eke V. R., Cole S., Frenk C. S., 1996, MNRAS, 282, 263
Estrada J., Sefusatti E., Frieman J., 2009, ApJ, 692, 265
Ettori S., Fabian A. C., White D. A., 1997, MNRAS, 289, 787
Evrard A. E., MacFarland T. J., Couchman H. M. P. et al., 2002, ApJ, 573, 7
Fleenor M. C., Rose J. A., Christiansen W. A., Hunstead R. W., Johnston-Hollitt M., Drinkwater M. J., Saunders W., 2005, AJ, 130, 957
Governato F., Babul A., Quinn T., Tozzi P., Baugh C. M., Katz N., Lake G., 1999, MNRAS, 307, 949
Gunn J. E., Gott J. R. I., 1972, ApJ, 176, 1
Giovanelli R., Haynes M. P., Chincarini G. L., 1986, ApJ, 300, 77
Heath D. J., 1977, MNRAS, 179, 351
Hoffman Y., Lahav O., Yepes G., Dover Y., 2007, J. Cosmol. Astropart. Phys., 10, 16
Icke V., 1973, A&A, 27, 1
Jenkins A., Frenk C. S., White S. D. M., Colberg J. M., Cole S., Evrard A. E., Couchman H. M. P., Yoshida N., 2001, MNRAS, 321, 372
Jing Y. P., Suto Y., 2002, ApJ, 574, 538
Jones D. H. et al. 2009, MNRAS, submitted (arXiv:0903.5451)
Kaiser N., 1984, ApJ, 284, L9
Kasun S. F., Evrard A. E., 2005, ApJ, 629, 781
Katz N., 1991, ApJ, 368, 325
Kitayama T., Suto Y., 1996, ApJ, 469, 480
Kocevski D. D., Ebeling H., 2006, ApJ, 645, 1043
Lacey C., Cole S., 1993, MNRAS, 262, 627
Lahav O., Lilje P. B., Primack J. R., Rees M. J., 1991, MNRAS, 251, 128
Landau L. D., Lifshitz E. M., 1960, Mechanics. Pergamom Press, Oxford

Lilje P. B., Lahav O., 1991, ApJ, 374, 29
Lynden-Bell D., 1964, ApJ, 139, 1195
Mota D. F., van de Bruck C., 2004, A&A, 421, 71
Muñoz J. A., Loeb A., 2008, MNRAS, 391, 1341
Nagamine K., Loeb A., 2003, New Astron., 8, 439
Navarro J. F., Frenk C. S., White S. D. M., 1997, ApJ, 490, 493
Oort J. H., 1983, ARA&A, 21, 373
Paz D. J., Lambas D. G., Padilla N., Merchán M., 2006, MNRAS, 366, 1503
Peacock J. A., Heavens A. F., 1985, MNRAS, 217, 805
Peacock J. A., Heavens A. F., 1990, MNRAS, 243, 133
Peacock J. A., West M. J., 1992, MNRAS, 259, 494
Peebles P. J. E., 1980, The Large-Scale Structure of the Universe (Research Supported by the National Science Foundation. Princeton, NJ). Princeton University Press, Princeton, NJ, p. 435
Peebles P. J. E., 1984, ApJ, 284, 439
Plionis M., Valdarnini R., 1991, MNRAS, 249, 46
Plionis M., Valdarnini R., Jing Y.-P., 1992, ApJ, 398, 12
Press W. H., Schechter P., 1974, ApJ, 187, 425
Proust D. et al., 2006, A&A, 447, 133
Quintana H., Carrasco E. R., Reisenegger A., 2000, AJ, 120, 511
Raychaudhury S., 1989, Nat, 342, 251
Sathyaprakash B. S., Sahni V., Shandarin S. F., 1996, ApJ, 462, 5
Sathyaprakash B. S., Sahni V., Shandarin S. F., 1998, ApJ, 508, 551
Shandarin S. F., Zeldovich Ya. B., 1989, Rev. Mod. Phys., 61, 185
Shandarin S. F., Sheth J. V., Sahni V., 2004, MNRAS, 353, 162
Shapley H., Ames A., 1930, Harvard Coll. Obs. Bull., 880, 1
Sheth R. K., 1998, MNRAS, 300, 1057
Sheth R. K., Tormen G., 1999, MNRAS, 308, 119
Sheth R. K., Tormen G., 2002, MNRAS, 329, 61
Sheth J. V., Sahni V., Shandarin S. F., Sathyaprakash B. S., 2003, MNRAS, 343, 22
Springel V., 2005, MNRAS, 364, 1105
Springel V. et al., 2005, Nat, 435, 629
Szalay A. S., Schramm D. N., 1985, Nat, 314, 718
van de Weygaert R., Bond J. R., 2008, in Plionis M., Lopez-Cruz O., Hughes D., eds, A Pan-Chromatic View of Clusters of Galaxies and the Large-Scale Structure. Lect. Notes Phys. Vol. 740. Springer, Dordrecht, p. 335
van Haarlem M., van de Weygaert R., 1993, ApJ, 418, 544
White S. D. M., Silk J., 1979, ApJ, 231, 1
Wray J. J., Bahcall N. A., Bode P., Boettiger C., Hopkins P. F., 2006, ApJ, 652, 907
Zeldovich Ya. B., 1970, A&A, 5, 84
Zeldovich Ya. B., Einasto J., Shandarin S. F., 1982, Nat, 300, 407

APPENDIX A: LINEAR DENSITY EXCESS OF CRITICAL SHELL

In order to find the linear density excess δ_0 for the critically bound shell, we evaluate its evolution at early epochs ($a \ll 1$). At these early times – when density perturbations are still very small, $\delta \ll 1$ – the linearly extrapolated density excess (equation 15),

$$\delta(a) = D(a)\,\delta_0, \tag{A1}$$

represents a good approximation for the (real) density of the object (equation 13).

At early times, the Universe is very close to an Einstein–de Sitter Universe, expanding according to

$$a(t) = \left(\frac{t}{t_*}\right)^{2/3}, \tag{A2}$$

where t_* is the characteristic expansion time.

Following this cosmic evolution,

$$1 + \delta \equiv \frac{\rho}{\rho_u} = \frac{2\Omega_{\Lambda 0}}{\Omega_{m,0}} \left(\frac{a}{\tilde{r}}\right)^3, \tag{A3}$$

to first order yields

$$\frac{t(\tilde{r})}{\tilde{r}^{3/2}} \approx t_* \left(1 + \frac{\delta}{2}\right) \left(\frac{\Omega_{m,0}}{2\Omega_{\Lambda,0}}\right)^{1/2}. \tag{A4}$$

This approximation, neglecting contributions of order δ^2 and higher, is reasonably accurate for density perturbations $\delta \ll 1$. The evolution of the critical shell's radius $\tilde{r}(t)$, the solution to the energy equation (5) for $\tilde{E} = \tilde{E}^* = -\frac{3}{2}$, is given by the integral expression

$$\tilde{t} = \int_0^{\tilde{r}} \frac{\sqrt{r}\,dr}{(1-r)\sqrt{r+2}}. \tag{A5}$$

Retaining the two lowest order terms of this equation,

$$t(\tilde{r}) \approx \sqrt{\frac{2}{3\Lambda}}\,\tilde{r}^{3/2} + \frac{3}{10}\sqrt{\frac{3}{2\Lambda}}\,\tilde{r}^{5/2}, \tag{A6}$$

we find that

$$\frac{t}{\tilde{r}^{3/2}} \approx \sqrt{\frac{2}{3\Lambda}}\left(1 + \frac{9}{20}\tilde{r}\right). \tag{A7}$$

The front factor on the right-hand side of this equation should be equal to that of equation (A4), so that the characteristic time t_* is found to be

$$t_* = \left[\frac{4\Omega_{\Lambda,0}}{3\Lambda\Omega_{m,0}}\right]^{1/2}. \tag{A8}$$

Combining expression (A6) with that of equation (A4) we find that

$$t_*\left(1 + \frac{\delta}{2}\right)\left(\frac{\Omega_{m,0}}{2\Omega_{\Lambda,0}}\right)^{1/2} \approx \sqrt{\frac{2}{3\Lambda}}\left(1 + \frac{9}{20}\tilde{r}\right), \tag{A9}$$

resulting in the following relation between the early density excess of the bound sphere and its dimensionless radius $\tilde{r}$:

$$\delta(t) = \frac{9}{10}\,\tilde{r}(t). \tag{A10}$$

APPENDIX B: PRESS–SCHECHTER MODELLING OF SUPERCLUSTERS

According to the Press–Schechter formalism (Press & Schechter 1974; Peacock & Heavens 1990; Bond et al. 1991; Sheth 1998), the comoving number density of haloes of mass M at redshift z, in a cosmic background of density ρ_u, is given by the expression

$$\frac{dn}{dM} = \sqrt{\frac{2}{\pi}}\,\frac{\rho_u}{M^2}\,\frac{\delta_c}{\sigma(M,z)}\left|\frac{d\ln\sigma(M,z)}{d\ln M}\right|e^{\frac{-\delta_c^2}{2\sigma^2(M,z)}}, \tag{B1}$$

in which δ_c/σ quantifies the relative critical overdensity δ_c of collapse with respect to the variance of density fluctuations $\sigma(M,z)$ on a mass scale M. For a scenario with a power spectrum $P(k)$ of the linear density field,

$$\sigma^2(M) = 4\pi \int_0^\infty P(k)\omega(kr)k^2\,dk, \tag{B2}$$

where $\omega(kr)$ is the Fourier-space representation of a real-space top-hat filter enclosing a mass M in a radius r at the mean density of the Universe, which is given by

$$\omega(kr) = 3\left[\frac{\sin(kr)}{(kr)^3} - \frac{\cos(kr)}{(kr)^2}\right]. \tag{B3}$$

The critical spherical collapse overdensity value δ_c has a weak dependence on the cosmological background (Gunn & Gott 1972; Lacey & Cole 1993; Eke et al. 1996; Kitayama & Suto 1996). Useful fitting formulae for the linear spherical model collapse value δ_c were

obtained by Navarro et al. (1997) for $\Omega_\Lambda = 0$ FRW Universes and for flat Universes,

$$\delta_c(\Omega_m) = \begin{cases} 0.15(12\pi)^{2/3}\Omega_m^{0.0185} & \Omega_m < 1, \Omega_\Lambda = 0, \\ 0.15(12\pi)^{2/3}\Omega_m^{0.0055} & \Omega_m + \Omega_\Lambda = 1. \end{cases} \quad \text{(B4)}$$

According to this formula $\delta_c = 1.68$ at $a = 1$ (for $\Omega_m = 0.3$), while at $a = 100$, when $\Omega_m = 0.43 \times 01^{-6}$, one finds $\delta_c = 1.56$. A similar expression for the critical virial density has been given by Bryan & Norman (1998),

$$\Delta_{\text{vir}} = \begin{cases} 18\pi^2 + 82(\Omega_m - 1) - 39(\Omega_m - 1)^2 \\ \qquad\qquad\qquad\qquad \Omega_m + \Omega_\Lambda = 1 \\ 18\pi^2 + 60(\Omega_m - 1) - 32(\Omega_m - 1)^2 \\ \qquad\qquad\qquad\qquad \Omega_m < 1, \Omega_\Lambda = 0. \end{cases} \quad \text{(B5)}$$

While most applications of the (extended) PS formalism assume perfectly spherical collapse, we know that generic gravitational collapse of primordial density peaks proceeds anisotropically. Sheth & Tormen (1999) improved the PS formalism by taking into account the anisotropic collapse implied by the anisotropic primordial shape of density peaks and the anisotropic tidal stresses imparted by external mass concentrations. Modelling this by means of the ellipsoidal collapse model (e.g. Lynden-Bell 1964; Icke 1973; White & Silk 1979; Eisenstein & Loeb 1995; Bond & Myers 1996; Desjacques 2008) they showed this translates into a more fuzzy *moving collapse density barrier*. The resulting mass function,

$$\frac{dn_{\text{ST}}}{dM} = A\sqrt{\frac{2a}{\pi}}\left[1 + \left(\frac{\sigma(M)^2}{a\delta_c^2}\right)^p\right]\frac{\rho_u}{M^2}\frac{\delta_c}{\sigma(M)}$$
$$\times \left|\frac{d\ln\sigma(M)}{d\ln M}\right| e^{\frac{-a\delta_c^2}{2\sigma^2(M)}}, \quad \text{(B6)}$$

with $a = 0.707$, $p = 0.3$ and $A \approx 0.322$, gives a substantially better fit to the mass functions obtained in N-body simulations. In comparison with the standard PS mass function, ST predicts a higher abundance of massive objects and a smaller number of less massive ones. Later, Jenkins et al. (2001) reported a small disagreement with respect to N-body simulations: underpredictions for the massive haloes and overpredictions for the less massive haloes. They suggested the alternative expression

$$\frac{dn_J}{dM} = A\frac{\rho_u}{M^2}\frac{d\ln\sigma(M)}{d\ln M}e^{(-|\ln\sigma^{-1}+B|)^\epsilon} \quad \text{(B7)}$$

with $A = 0.315$, $B = 0.61$ and $\epsilon = 3.8$. Note, however, that their expression does not depend explicitly on δ_c. They showed that 'for a range of CDM cosmologies and for a suitable halo definition, the simulated mass function is almost independent of epoch, of cosmological parameters and of initial power spectrum'.

This paper has been typeset from a TEX/LATEX file prepared by the author.